Supporting Information

Mechanism by which Nitrous Oxide Enables Continuous Methane Hydroxylation on Fe-CHA Zeolites

Daniel C. Cano-Blanco[1,2], Jailyn George[3], Jörg. W. A. Fischer[4, 5], Zequan Li[1,2], Gabriela-Teodora Dutcă[1,2], Daniele Bonavia[6], Adam H. Clark[6], Maarten Nachtegaal[1, 6, 7], Wenshuo Hu[3*], Oliver Kröcher[1,2], Davide Ferri[1*]

[1] PSI Center for Energy and Environmental Sciences, Paul Scherrer Institute, CH-5232 Villigen PSI, Switzerland

[2] Institute of Chemical and Bioengineering, École polytechnique fédérale de Lausanne (EPFL), CH-1015 Lausanne, Switzerland

[3] Department of Chemical Engineering, Edward E. Whitacre Jr. College of Engineering, Texas Tech University, Lubbock, TX 79409, United States

[4] Institute for Molecular Physical Science, ETH Zurich, Vladimir-Prelog-Weg 1–5/10, 8093 Zurich, Switzerland

[5] Inorganic Chemistry and Catalysis, Debye Institute for Nanomaterials Science and Institute for Sustainable and Circular Chemistry, Faculty of Science, Utrecht University, Utrecht, The Netherlands

[6] PSI Center for Photon Science, Paul Scherrer Institute, CH-5232 Villigen PSI, Switzerland

[7] Institute for Inorganic Chemistry, ETH Zurich, Vladimir-Prelog-Weg 1–5/10, 8093 Zurich, Switzerland

* Corresponding authors

wenshuo.hu@ttu.edu (W. Hu); davide.ferri@psi.ch (D. Ferri)

Table of Contents

Supplementary Note 1

Pre-edge subtraction and analysis from Fe Kα HERFD-XANES

In analogy to Wilke et al.[1] and Boubnov et al.[2], the enhanced spectral resolution provided by Fe Kα high-energy-resolution fluorescence-detected XANES (HERFD-XANES) was exploited to extract quantitative information from the pre-edge region. To isolate the pre-edge contribution, the background was modeled and subtracted using an arctangent function describing the absorption edge:

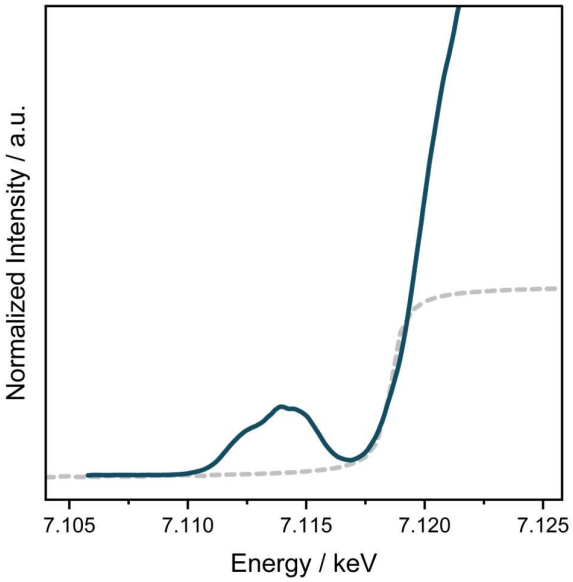

Pre-edge subtraction from Fe Kα HERFD-XANES. The experimental spectrum (solid curve) is modeled with an arctangent function describing the absorption edge (dashed curve).

The resulting pre-edge feature was then fitted using a sum of Gaussian functions, and the number of components was chosen to obtain an optimal description of the experimental data. From both the raw and fitted pre-edge, the integrated pre-edge intensity was determined from the peak area, and the centroid position was calculated. Reference compounds with well-defined Fe oxidation states and coordination environments were used for calibration of the

centroid position analysis: $FePO_4 \cdot 2H_2O$ (Fe^{3+}, octahedral), Fe_2O_3 (Fe^{3+}, octahedral), $FePO_4$ (Fe^{3+}, tetrahedral), and $FeSO_4 \cdot 7H_2O$ (Fe^{2+}, octahedral). The pre-edge analysis enables a quantitative estimation of the average Fe redox state, leveraging the linear relationship between the centroid position and the oxidation state.[3]

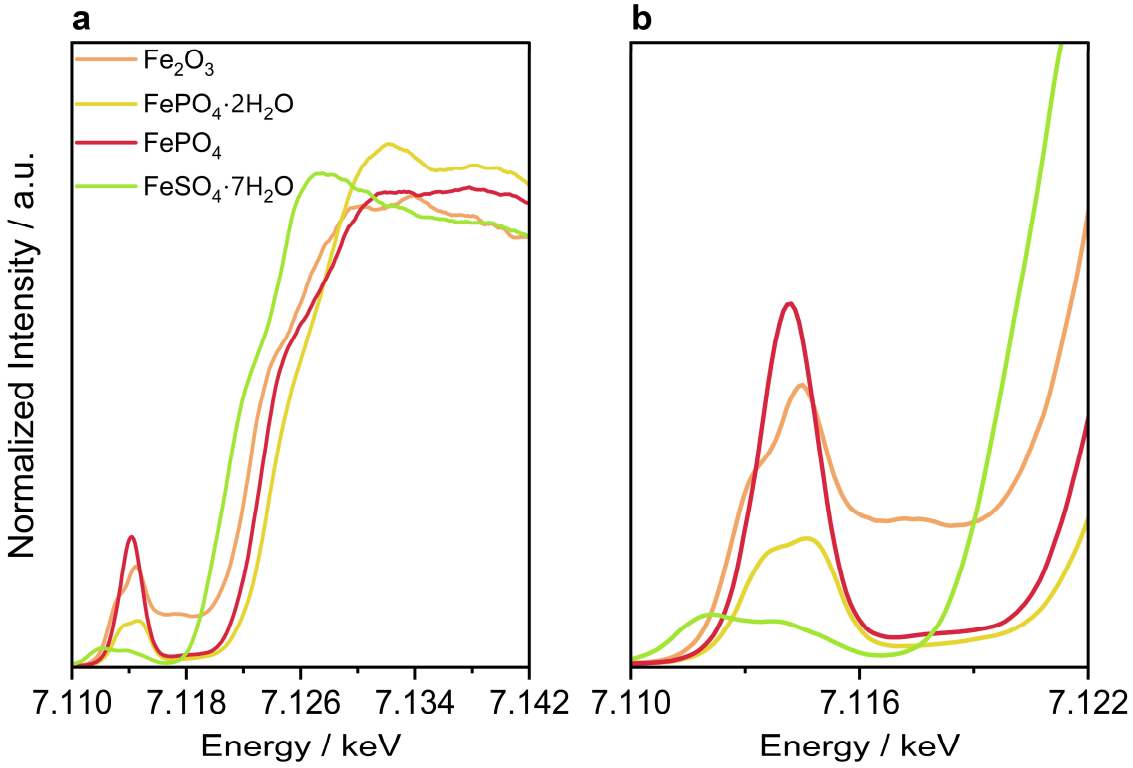

Fe Kα HERFD-XANES reference spectra used for pre-edge calibration. a, Normalized HERFD-XANES of $FePO_4 \cdot 2H_2O$ (Fe^{3+}, octahedral), Fe_2O_3 (Fe^{3+}, octahedral), $FePO_4$ (Fe^{3+}, tetrahedral), and $FeSO_4 \cdot 7H_2O$ (Fe^{2+}, octahedral). **b,** Magnified view of the pre-edge region.

It is important to emphasize that pre-edge analysis alone cannot unambiguously determine the coordination geometry of Fe^{2+} and Fe^{3+}, particularly when the system deviates from ideal symmetries. This limitation is especially relevant for Fe sites in zeolites, where a range of local environments can arise due to varying anchoring sites and degrees of speciation.[3]

Supplementary Note 2

Multivariate curve resolution (MCR)

Applying the multivariate curve resolution-alternating least squares (MCR-ALS) method to decompose the time-resolved *operando* XANES data of Fe-CHA, three significant components (**Fig. 6g**; lack of fit presented in **Supplementary Figure 23**) associated with Fe centers were identified over the whole reaction protocol and captured most of the signal variance: an oxidized component formed upon contact with N_2O (Component 1), and two reduced components (Components 2 and 3) observed under CH_4 and N_2O+CH_4. The absorption edge energies of these components, determined at a normalized intensity of 0.9, were correlated with the formal Fe oxidation-state analysis reported in **Supplementary Figure 6**, following an approach analogous to previous studies.[4, 5] The linear correlation between edge energy and average oxidation state was derived from Fe^{2+} and Fe^{3+} reference compounds, yielding average oxidation states of 2.9 for Component 1, 2.2 for Component 2, and 2.1 for Component 3.

Accordingly, Component 1 is assigned predominantly to Fe^{3+} species in Fe-CHA, whereas Components 2 and 3 are assigned predominantly to Fe^{2+} species. The latter two components differ mainly in the local coordination environment of Fe, as indicated by the feature at 7.120 keV in Component 2, which is characteristic of square-planar Fe^{2+} species, as discussed in the main text. Since the kinetic analysis focused on the evolution of Fe oxidation states, Components 2 and 3 were combined into a single contribution representative of Fe^{2+} species for the analysis shown in **Fig. 6h**.

Supplementary Note 3

Additional details on density functional theory calculations

Hexagonal CHA unit cells containing 36 tetrahedral (T) sites were taken from the International Zeolite Association (IZA) database (13.675×13.675×14.767, unit: Å)[6] and used to model the CHA framework studied in the present work. Two Si atoms within the same six-membered ring (6MR), separated by two intervening T sites, were substituted by Al (denoted Z_2, where Z indicates CHA and "2" denotes two Al atoms per unit cell), giving a Si/Al ratio of 17/1, comparable to that of the CHA catalysts used experimentally. This Al arrangement stabilizes isolated Fe^{2+} cations in a square-planar coordination environment (Z_2Fe^{2+}, **Supplementary Fig. 26a**), which is energetically preferred[7, 8] and consistent with the spectroscopic evidence reported in the main text.

Periodic, spin-polarized DFT calculations were performed with the *Vienna Ab initio Simulation Package* (VASP 6.5.1)[9, 10] and the projector-augmented wave (PAW) method, using a plane-wave cutoff of 400 eV. Geometries were first relaxed with the Perdew−Burke−Ernzerhof (PBE)[11] functional, including a Hubbard correction (U= 3 eV) on Fe[12] within the Dudarev scheme[13] (PBE+U); they were then refined using the hybrid Heyd−Scuseria−Ernzerhof (HSE)[14, 15, 16] functional, with the fraction of Hartree−Fock exchange set to 0.15, following prior calibrations for Fe-containing systems.[12, 17] In both stages, dispersive corrections by DFT-D3 with Becke−Johnson (BJ) damping[18, 19] were applied. Total energies and forces were converged to 10^{-6} eV and 0.03 eV·Å^{-1}, respectively, with the first Brillouin zone sampled at the Γ-point. The partial charges of Fe were obtained from Bader analysis[20, 21, 22] and normalized against Fe^{2+} and Fe^{3+} reference structures to estimate effective oxidation states. The Fe^{2+} reference is Z_2Fe^{2+} (**Supplementary Fig. 26a**), in which Fe compensates the two framework negative charges introduced by two Al substitutions; the Fe^{3+} reference is $Z_2Fe^{3+}OH$

(**Supplementary Fig. 26b**), in which Fe additionally compensates the negative charge associated with the hydroxyl group.[17]

Vibrational frequencies were computed for the PBE+*U* (+ D3-BJ) optimized structures at the same level of theory using the finite-difference method with a displacement of 0.015 Å. The resulting frequencies were used to obtain zero-point vibrational energies (ZPE) and to derive enthalpies (H), entropies (S), and free energies (G) according to:[23]

$$H = E_0 + \mathrm{ZPE} + H_{\mathrm{trans}} + H_{\mathrm{rot}} + H_{\mathrm{vib}} \quad \textbf{(S1)}$$

$$G = H - T \cdot \left[\frac{2}{3} \cdot \left(S_{\mathrm{trans}}^{\mathrm{gas}} + S_{\mathrm{rot}}^{\mathrm{gas}}\right) + S_{\mathrm{vib}}^{\mathrm{zeo}}\right] \quad \textbf{(S2)}$$

Here, E_0 is the DFT-calculated electronic energy (including dispersion). The subscripts "trans", "rot", and "vib" denote translational, rotational, and vibrational contributions derived from standard statistical mechanics formalisms.[24] Low-frequency modes often correspond to frustrated translations/rotations of the zeolite-confined species or framework and can disproportionately affect entropy estimates ($S_{\mathrm{vib}}^{\mathrm{zeo}}$). Therefore, frequencies below 100 cm^{-1} were set to 100 cm^{-1}, except for modes corresponding to motion along the reaction coordinate for transition states.[25, 26] For mobile molecules confined within the CHA cages (e.g., N_2O, CH_4, CH_3OH, and N_2), partial translational and rotational freedom was retained by approximating these contributions as 2/3 of the corresponding gas-phase entropies ($S_{\mathrm{trans}}^{\mathrm{gas}}$ and $S_{\mathrm{rot}}^{\mathrm{gas}}$, Eq. S2), consistent with prior theoretical treatments of CHA under comparable conditions.[23, 27, 28, 29]

Transition states were initially located using the nudged elastic band (NEB) method[30] at the PBE+*U* (+ D3-BJ) level, with total energies converged to 10^{-6} eV and atomic forces below 0.03 $\mathrm{eV \cdot Å^{-1}}$; they were then refined at the HSE level using the Dimer method[31] to the same convergence criteria. Transition states were confirmed by the detection of one imaginary frequency corresponding to the vibration along the reaction coordinate.

Supplementary Tables

Supplementary Table 1. Summary of reported catalytic performance for continuous N_2O-assisted CH_4 hydroxylation, including catalyst composition, reaction conditions, and reported oxygenate selectivity and formation rates.[a]

Catalyst	$r_{MeOH+DME}$[b] / μmol min^{-1} g_{Fe}^{-1}	$S_{MeOH+DME}$[c] / %	Conditions	Ref.
Fe-CHA (0.4%wt Fe)	274.4	92	275 °C, 0.5%vol N_2O, 1%vol CH_4, Ar bal., 60 mL min^{-1}, m_{cat} = 190 mg	this study
Fe-AEI (1.5%wt Fe)	267	85	250 °C, $CH_4/N_2O/H_2O/Ar$ = 10:10:2:3, 25 mL min^{-1}, m_{cat} = 100 mg	[32]
Fe-MOR[d] (1.9 wt%)	301.2	25	300 °C, $CH_4/N_2O/H_2O$ = 30:10:11-18, He bal., 100 mL min^{-1}, m_{cat} = 300 mg	[33]
Fe-SSZ-13[d] (1.4 wt%)	76.2	18	270 °C, $CH_4/N_2O/H_2O$ = 30:30:3, He bal, 50 mL min^{-1}, m_{cat} = 300 mg	[33]
Fe-SSZ-39[d] (1.6 wt%)	107.3	6		
Fe-FER[d] (1.5 wt%)	424.4	54		
Fe-ZSM-5[d] (0.75 wt%)	313.3	26		

Supplementary Table 1, continued.

Catalyst	$r_{MeOH+DME}$[b] / µmol min^{-1} g_{Fe}^{-1}	$S_{MeOH+DME}$[c] / %	Conditions	Ref.
Fe-FER[d] (0.5 wt%)	-	20	350 °C, $CH_4/N_2O/He$ = 28:7:65, He bal., 70 mL min^{-1}, m_{cat} = 200 mg	[34]
Fe-ZSM-5[d] (0.5 wt%)	-	4		
Fe-Beta[d] (0.5 wt%)	-	5		
Fe-ZSM-5[d] (2 wt%)	15.6	18.3	300 °C, 2%vol N_2O, 20%vol CH_4, Ar bal., 55 mL min^{-1}, m_{cat} = 440 mg	[35]
Fe-ZSM-5[d] (2 wt%)	-	1.9	300 °C, $CH_4/N_2O/He$ = 20:2:78, He bal., 30 mL min^{-1}, m_{cat} = 360 mg	[36]

[a] Literature data, as published, has been re-calculated in terms of mass-intrinsic activity.

[b] reaction rate.

[c] Selectivity.

[d] Selectivity and formation rate refer to MeOH only.

Supplementary Table 2. Summary of steady-state continuous N_2O-assisted CH_4 oxidation over Fe-CHA.

Temperature / °C	**Conversion / %**		**Rates / μmol min^{-1} g_{Fe}^{-1}**			
/	**N_2O**	**CH_4**	**N_2O**	**CH_4**	**MeOH**	**MeOH +DME**
275	2.44	1.02	416.18	298.48	41.98	274.37
300	6.13	3.07	1038.97	905.32	80.56	539.04
325	22.42	7.28	3798.18	2145.11	277.57	1200.86
350	45.21	13.37	7659.01	3936.54	532.15	1484.52

Supplementary Table 3. Summary of reaction conditions used in each *operando* spectroscopic measurement, including flow rate, gas concentration, temperature, and catalyst mass.

	XAS	HERFD	DRIFTS	EPR
Catalyst mass (mg)	39.6	40.3	30.7	14.2
Temperature (°C)	275			
Flow mL min^{-1}	60	60	60	10
Gas Concentrations *Stepwise* protocol	1 vol% N_2O, Ar balance → 2 vol% CH_4, Ar balance			
Gas Concentrations Co-feeding protocol	0.5 vol% N_2O, 1 vol% CH_4, Ar balance			

Supplementary Table 4. Summary of measurement parameters for HERFD-XAS, XAS, EPR, and DRIFTS, together with the modulation-excitation frequency and pulse sequence applied in the ME experiments.

	ME Experiment	**N_2O vs CH_4** with constant Ar flow	**CH_4 vs Ar** with constant N_2O flow
	Conc. N_2O / vol%	1 vs 0	0.5
	Conc. CH_4 / vol%	0 vs 2	1 vs 0
	Temperature / °C	275	
Kα-HERFD	Half-cycle time / min	10	
	Number of cycles / -	12	
	Time spectrum / s	20	
		7.105 – 7.130 keV	
Kβ-HERFD	Half-cycle time / min	10	
	Number of cycles / -	12	
	Time spectrum / s	45	
		7.100 – 7.150 keV	
EPR[a]	Half-cycle time / min	10	
	Number of cycles / -	12	
	Time spectrum / s	61	
		50 – 400 mT	
DRIFTS	Half-cycle time / min	10	
	Number of cycles / -	8	
	Time spectrum / s	7.5	
		4000 – 800 cm^{-1}	

Supplementary Figures

Supplementary Figure 1. *Ex situ* spectroscopic results of Fe-CHA: Diffuse-reflectance UV-vis (DRUV), EPR, and Fe K-edge XANES spectra collected at ambient conditions for Fe-CHA.

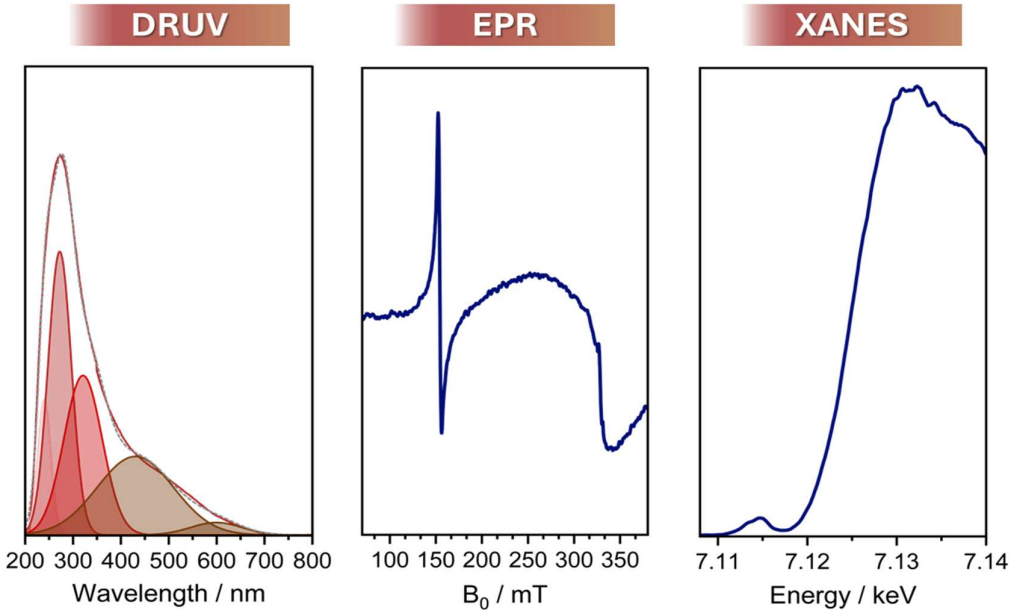

As previously reported,[37] the DRUV spectra were dominated by ligand-to-metal charge-transfer (LMCT) transitions associated with several Fe species: (i) tetrahedrally coordinated, isolated Fe^{3+} species within the zeolite framework (Td, 200-250 nm); (ii) extra-framework Fe^{3+} species, possibly in octahedral coordination (Oh, 250-300 nm); (iii) oligomeric extra-framework Fe^{3+} species confined within the zeolite pores (Fe_xO_y, 400-450 nm); and (iv) iron oxide particles located on the external surface of the zeolite (around 550-650 nm).

The EPR spectrum mainly revealed two types of Fe species: 1) resonances at $g' \approx 4.3$ and $g' \approx 8.8$ assigned to Fe centers located either in framework positions or at extra-framework sites; 2) the broad signal at $g' \approx 2$ attributed either to small Fe-oxide clusters (Fe_xO_y) or to highly symmetric isolated Fe^{3+} species.[37, 38]

The XANES spectrum is characterized by a pre-edge feature at 7.114 keV, typical of Fe^{3+} species, together with a shoulder at 7.112 keV, indicative of the co-presence of Fe^{2+} species.

Supplementary Figure 2. N_2O consumption rate (r_{N_2O}), CH_4 consumption rate (r_{CH_4}), and total oxygenate formation rate ($r_{MeOH+DME}$) as a function of temperature after exposing Fe-CHA to 1% N_2O for 30 min, followed by 30 min of 2% CH_4.

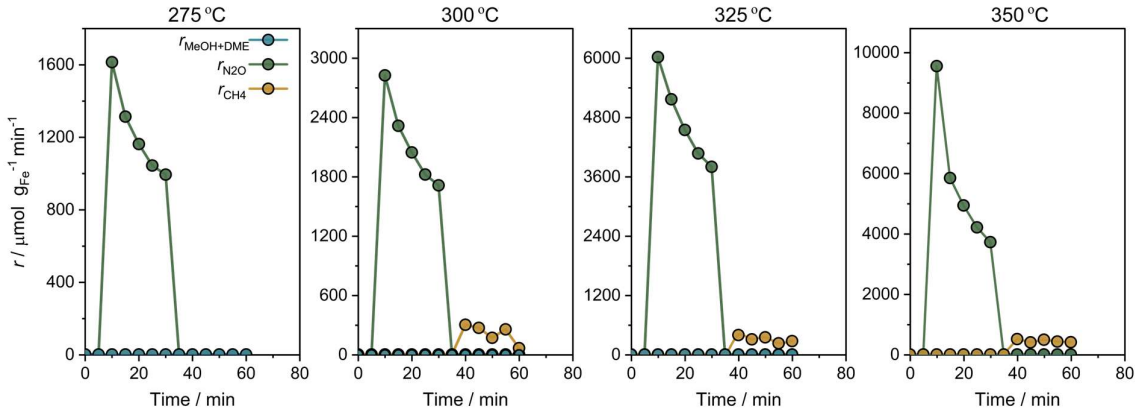

Supplementary Figure 3. N_2O consumption rate (r_{N_2O}), CH_4 consumption rate (r_{CH_4}), and total oxygenate formation rate ($r_{MeOH+DME}$) as a function of temperature during continuous exposure of Fe-CHA to a 0.5% N_2O + 1% CH_4 mixture for 130 min. Solid curves are shown to guide the eye.

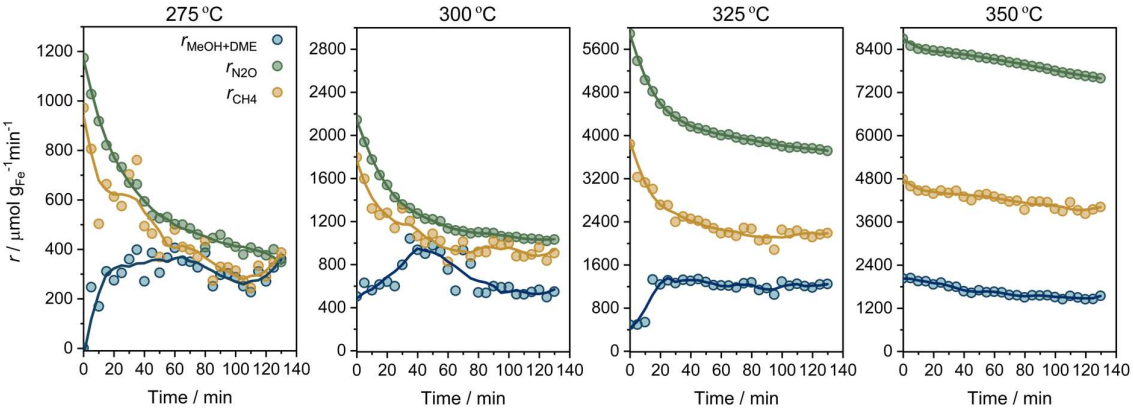

Supplementary Figure 4. Time-on-stream evolution of carbon-based product selectivity towards methanol (MeOH), dimethyl ether (DME), ethylene (C_2H_4), and CO_2 at the indicated temperatures.

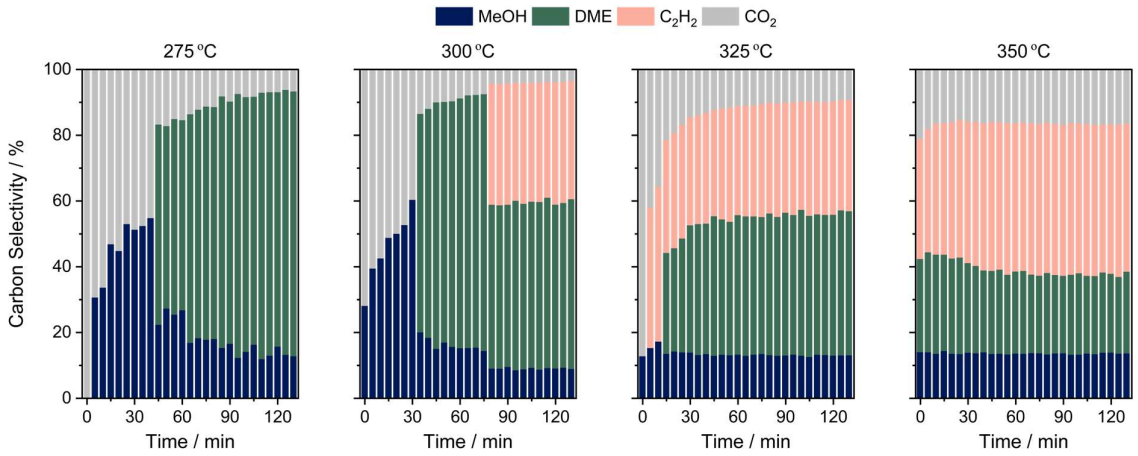

Supplementary Figure 5. First-order derivative of normalized absorbance and corresponding absorption edge energies for pristine Fe-CHA and upon dehydration from room temperature (RT) to 420°C. Experimental conditions: Ar flow (60 mL·min^{-1}), temperature ramp to 420°C (10°C·min^{-1}).

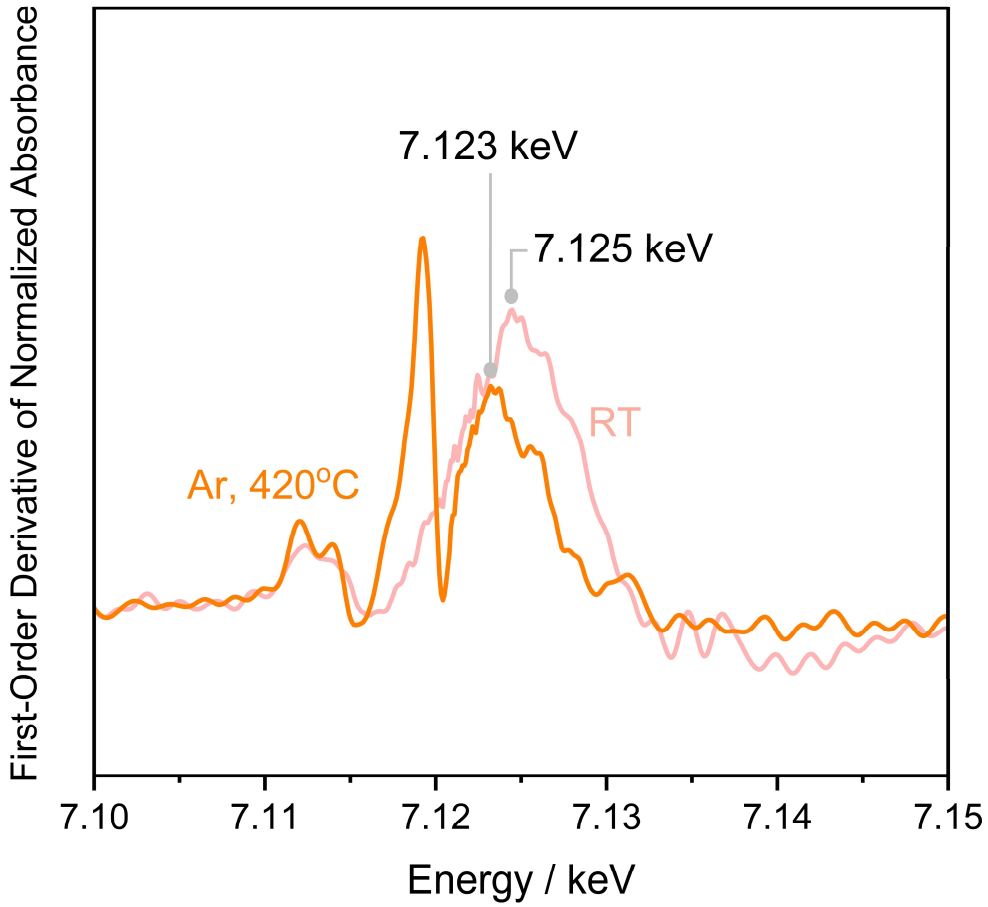

Supplementary Figure 6. a, Normalized Fe K-edge XANES spectra of reference compounds (FeO, Fe_2O_3, and $SrFeO_{3-x}$). **b,** Calibration of absorption energy at the normalized intensity of 0.9 versus formal Fe oxidation state. Experimental conditions: total flow rate of 60 $mL \cdot min^{-1}$, balanced in Ar, at 275°C, sequential exposure to N_2O (1 vol%) for 10 min, CH_4 (2 vol%) for 10 min, N_2O (0.5 vol%) + CH_4 (1 vol%) for 20 min, and finally Ar for 5 min.

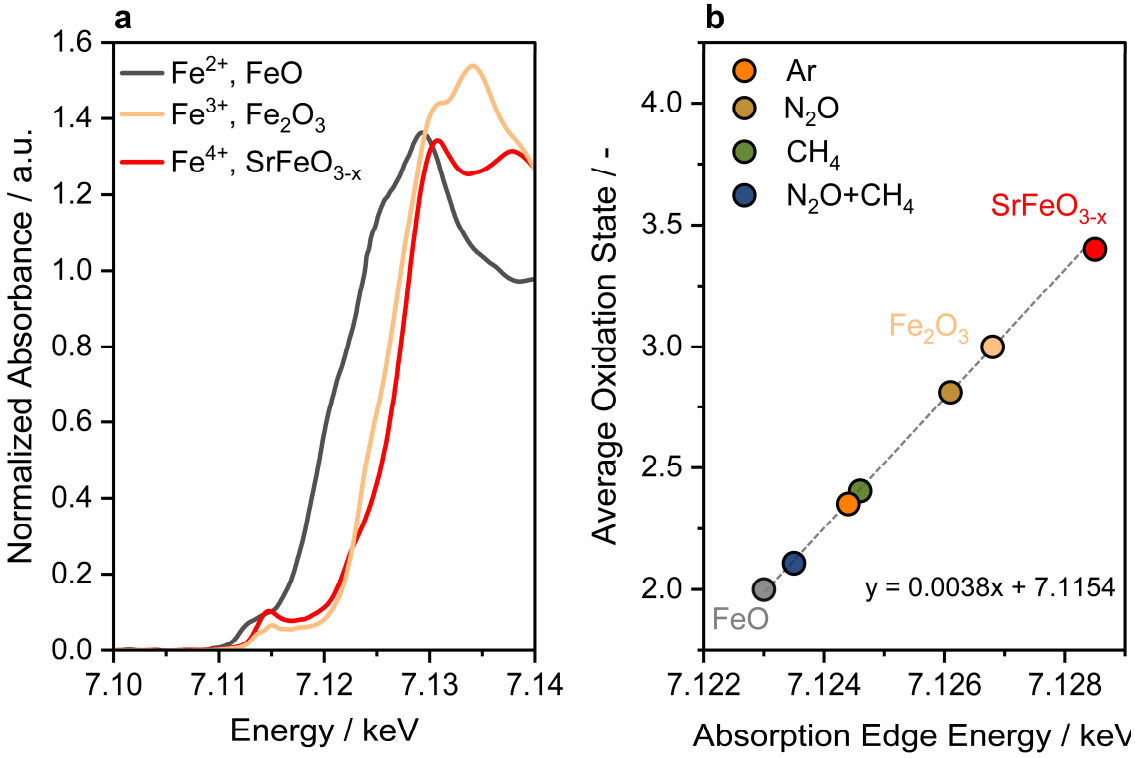

Absorption edge energies at the normalized intensity of 0.9 were plotted against formal Fe oxidation states, in analogous to previous analysis.[4, 5] The linear fit represents the correlation between edge energy and average oxidations state, derived from the Fe^{2+} and Fe^{3+} reference compounds.

Supplementary Figure 7. Evolution of the normalized ion current for the detected mass fragments m/z = 18 (H_2O) and m/z = 22 (carbon fragment used to monitor CO_2 formation) recorded during *operando* XAS (**Fig. 2a**) under dehydration conditions as a function of temperature. Experimental conditions: Ar flow (60 $mL \cdot min^{-1}$), temperature ramp to 420°C (10°C·min^{-1}).

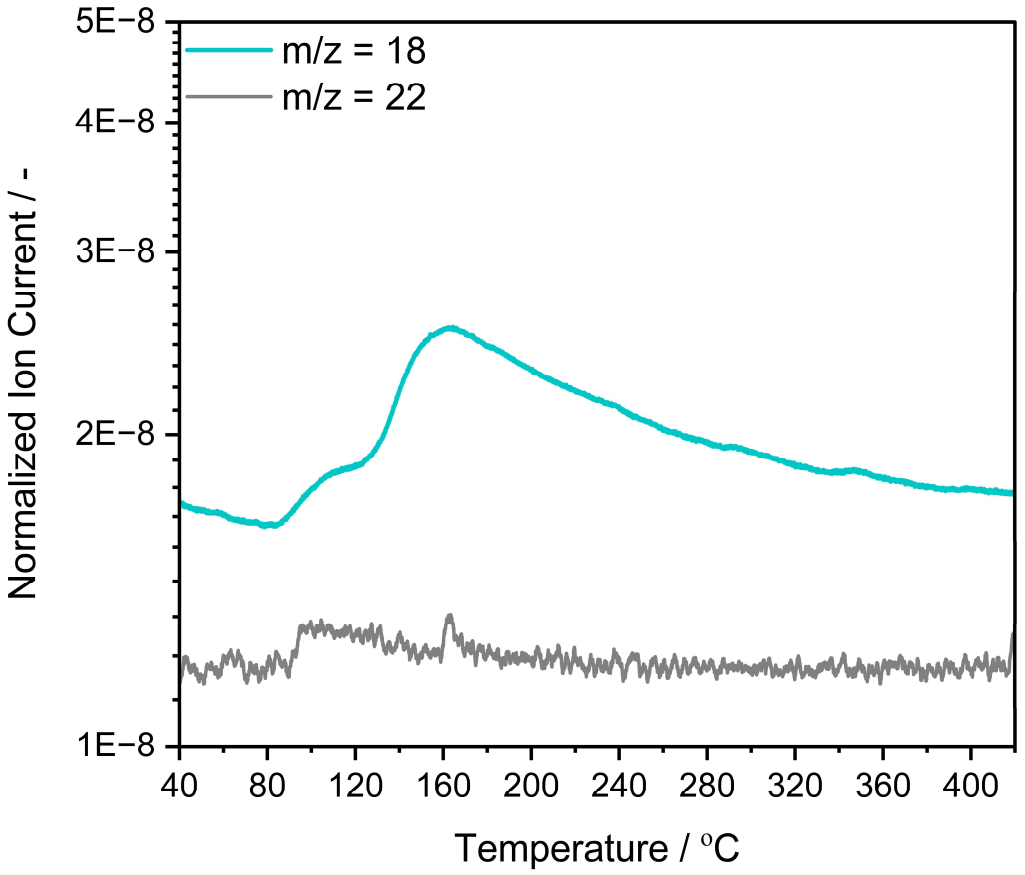

Supplementary Figure 8. a, Background-subtracted pre-edge features extracted from Fe-Kα-HERFD-XANES for pristine Fe-CHA and upon dehydration from room temperature (RT) to 420°C, along with corresponding Gaussian deconvolution fits. **b,** Pre-edge integrated intensity and centroid position of the spectra including reference compounds representative of Fe^{2+} and Fe^{3+} in Oh and Td coordination (**Supplementary Note 1**). Experimental conditions: Ar flow (60 mL·min^{-1}), temperature ramp to 420°C (10°C·min^{-1}).

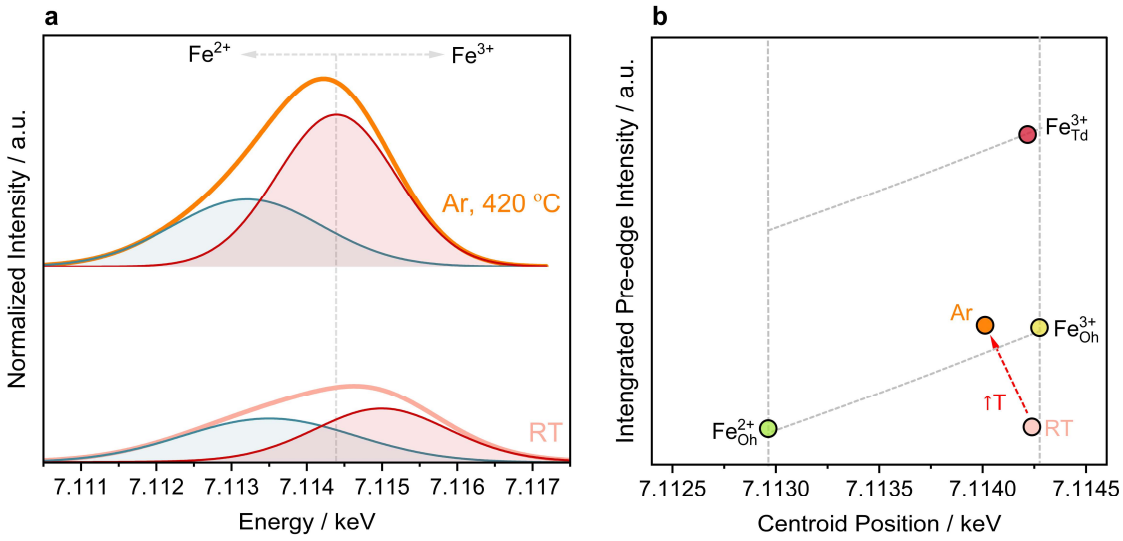

Supplementary Figure 9. a, 1*s*3*p* RIXS plane of Fe-CHA after dehydration at 420°C. **b**, Contant emission energy (CEE) cuts yielding Fe K-edge-like spectra. **c**, Fe $K\beta_{1,3}$ and Kβ' resonant XES spectra collected at constant incident energies (CIE). **d**, Non-resonant Fe Kβ XES spectra collected on Fe-CHA after dehydration at 420°C. Experimental conditions: Ar flow (60 mL·min^{-1}), temperature ramp to 420°C (10°C·min^{-1}).

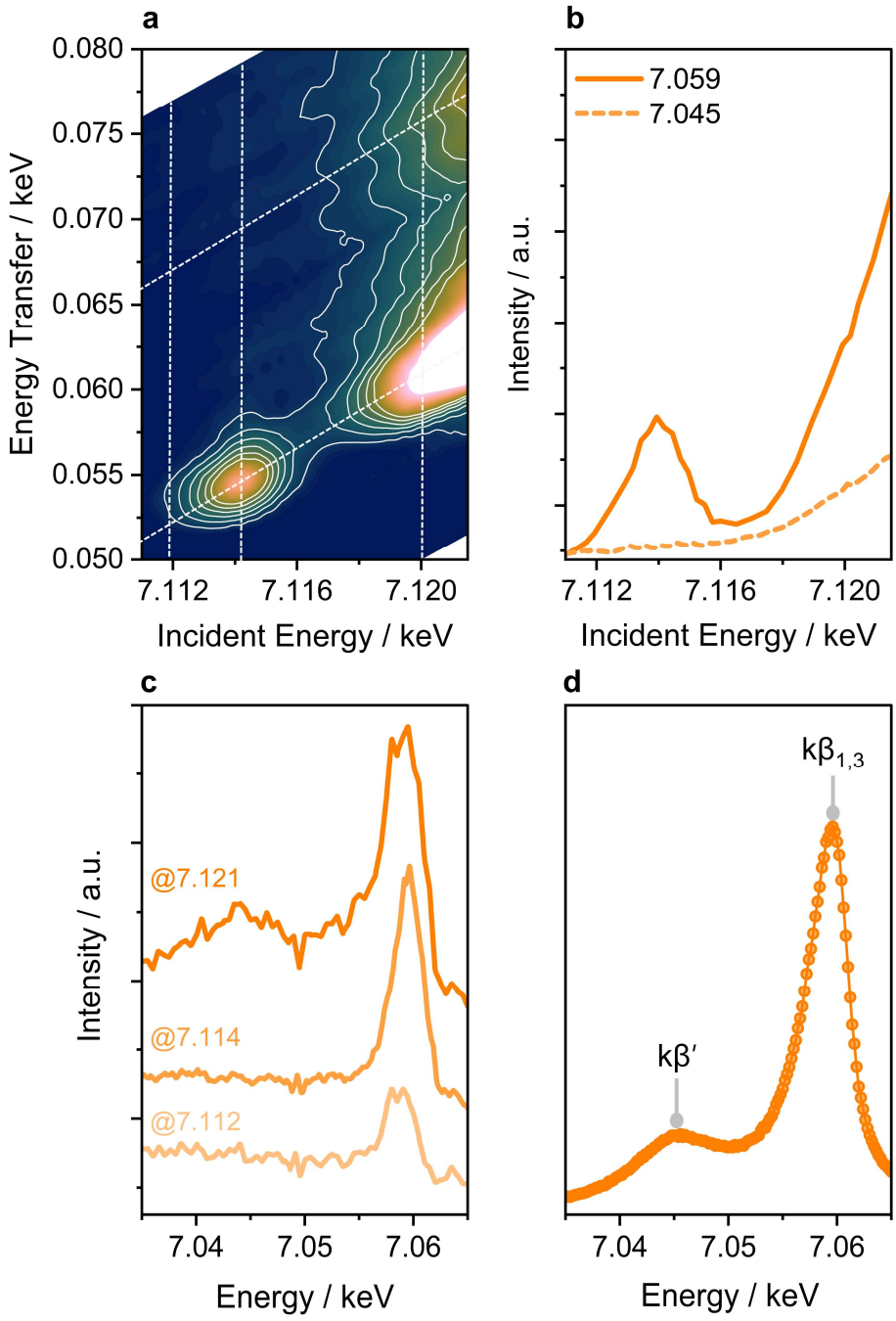

Supplementary Figure 10. Fe Kα-HERFD-XANES of Fe-CHA in different reaction environments. Experimental conditions: total flow rate of 60 mL·min^{-1}, balanced in Ar, at 275°C, sequential exposure to N_2O (1 vol%) for 10 min, CH_4 (2 vol%) for 10 min, N_2O (0.5 vol%) + CH_4 (1 vol%) for 20 min, and finally Ar for 5 min.

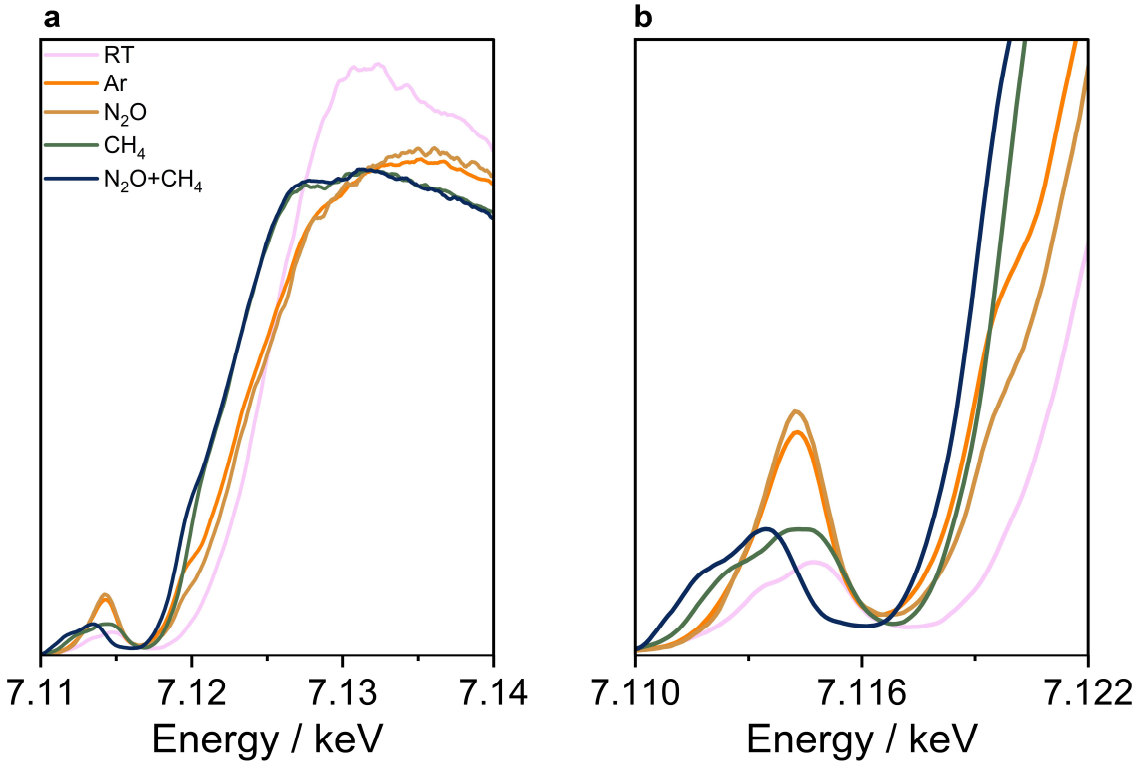

Supplementary Figure 11. Pre-edge integrated intensity and centroid position of the spectra from background subtracted Fe Kα-HERFD-XANES including reference compounds representative of Fe^{2+} and Fe^{3+} in Oh and Td coordination (**Supplementary Note 1**). Experimental conditions: total flow rate of 60 mL·min^{-1}, balanced in Ar, at 275°C, sequential exposure to N_2O (1 vol%) for 10 min, CH_4 (2 vol%) for 10 min, N_2O (0.5 vol%) + CH_4 (1 vol%) for 20 min, and finally Ar for 5 min.

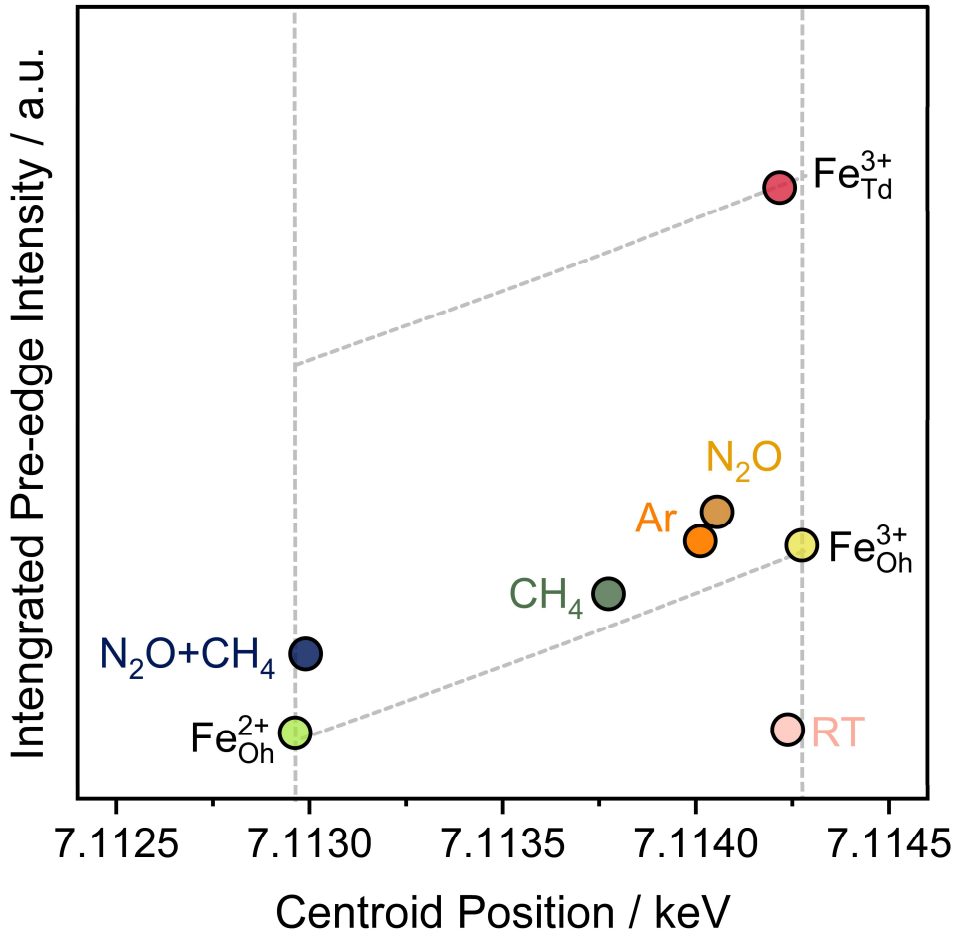

The pre-edge analysis provides an estimate of the average Fe oxidation state by exploiting the linear correlation between the pre-edge centroid energy and the Fe oxidation state. This correlation was calibrated using the Fe^{2+}_{Oh} and Fe^{3+}_{Oh} references, yielding the relationship $y = 0.0013x + 7.1103$, where y is the centroid energy and x is the formal Fe oxidation state.

Supplementary Figure 12. Bader-analysis-derived partial Fe charges vs the corresponding formal oxidation states of Fe species used as references (Z_2Fe^{2+} and $Z_2Fe^{3+}OH$) and relevant in CH_4 hydroxylation.

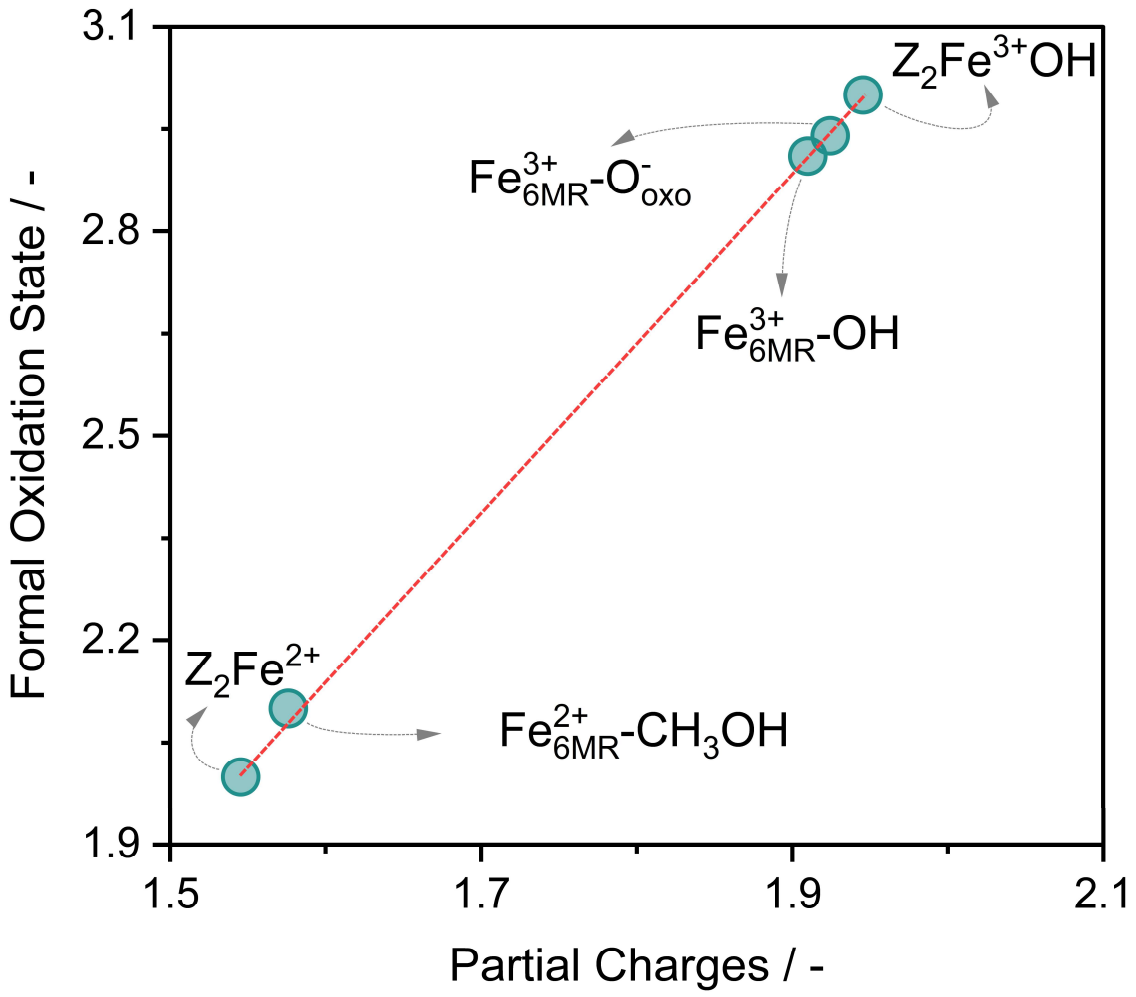

Supplementary Figure 13. Temporal evolution of the normalized ion current for the detected mass fragments m/z = 44 (N_2O), m/z = 28 (N_2), and m/z = 32 (O_2) during N_2O exposure in the *operando* XAS experiment (**Fig. 3a**). The inset highlights the transient behavior of the m/z = 28 signal. Experimental conditions: total flow rate of 60 mL·min^{-1}, balanced in Ar, at 275°C, exposure to N_2O (1 vol%) for 10 min.

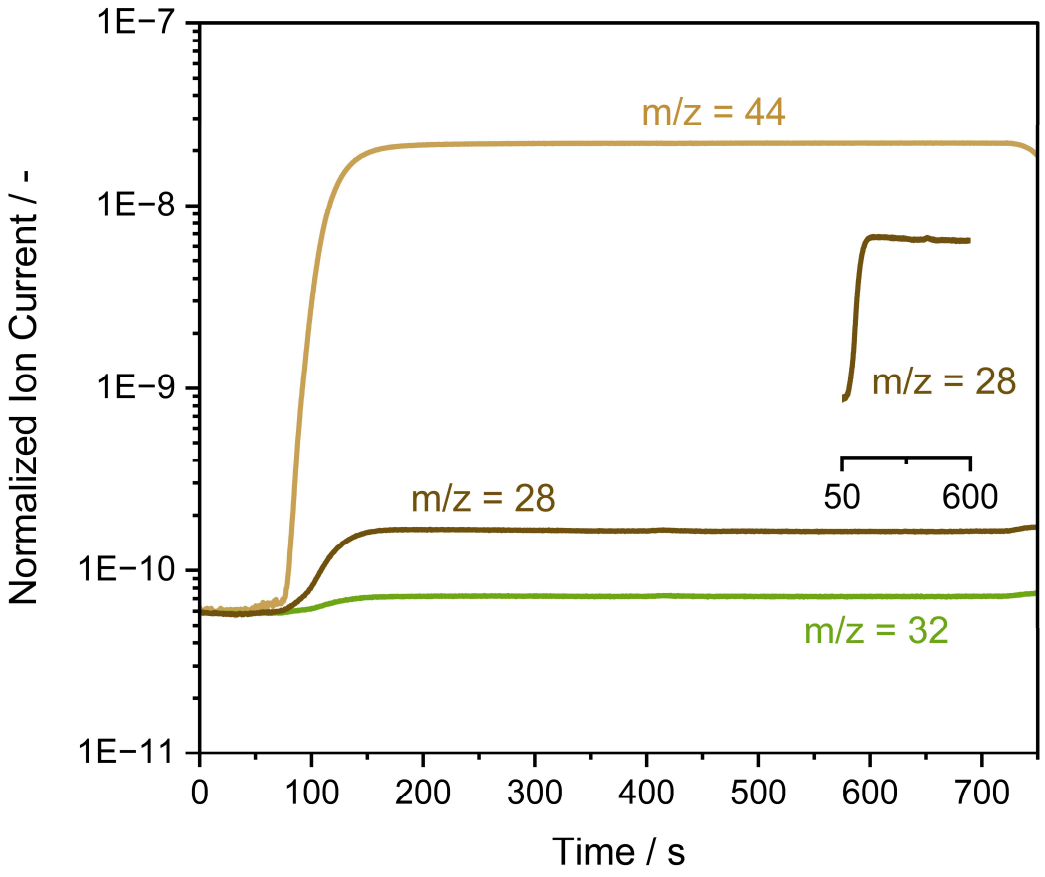

Supplementary Figure 14. a, Magnified view of the g' ≈ 2 region to emphasize variations in Fe-related paramagnetic signals. **b**, Differential EPR spectra obtained by subtracting the reference spectrum (as indicated). Experimental conditions: total flow rate of 60 mL·min^{-1}, balanced in Ar, at 275°C, sequential exposure to N_2O (1 vol%) for 10 min, CH_4 (2 vol%) for 10 min, N_2O (0.5 vol%) + CH_4 (1 vol%) for 20 min, and finally Ar for 5 min.

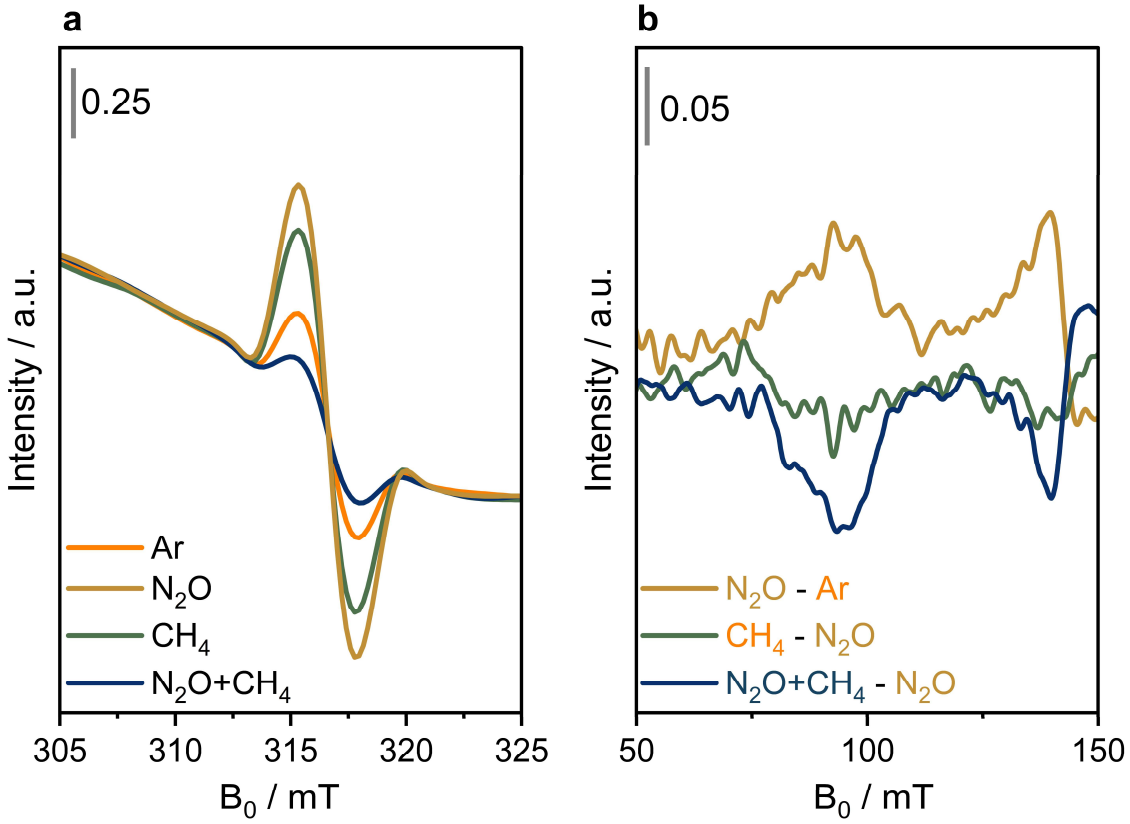

Supplementary Figure 15. 1*s*3*p* RIXS planes of Fe-CHA after the Ar treatment at 420 °C and upon contact with N_2O, along with their Fe K-edge-like spectra obtained by constant emission energy (CEE) cuts. Experimental conditions: total flow rate of 60 mL·min^{-1}, balanced in Ar, at 275°C, exposure to N_2O (1 vol%) for 10 min.

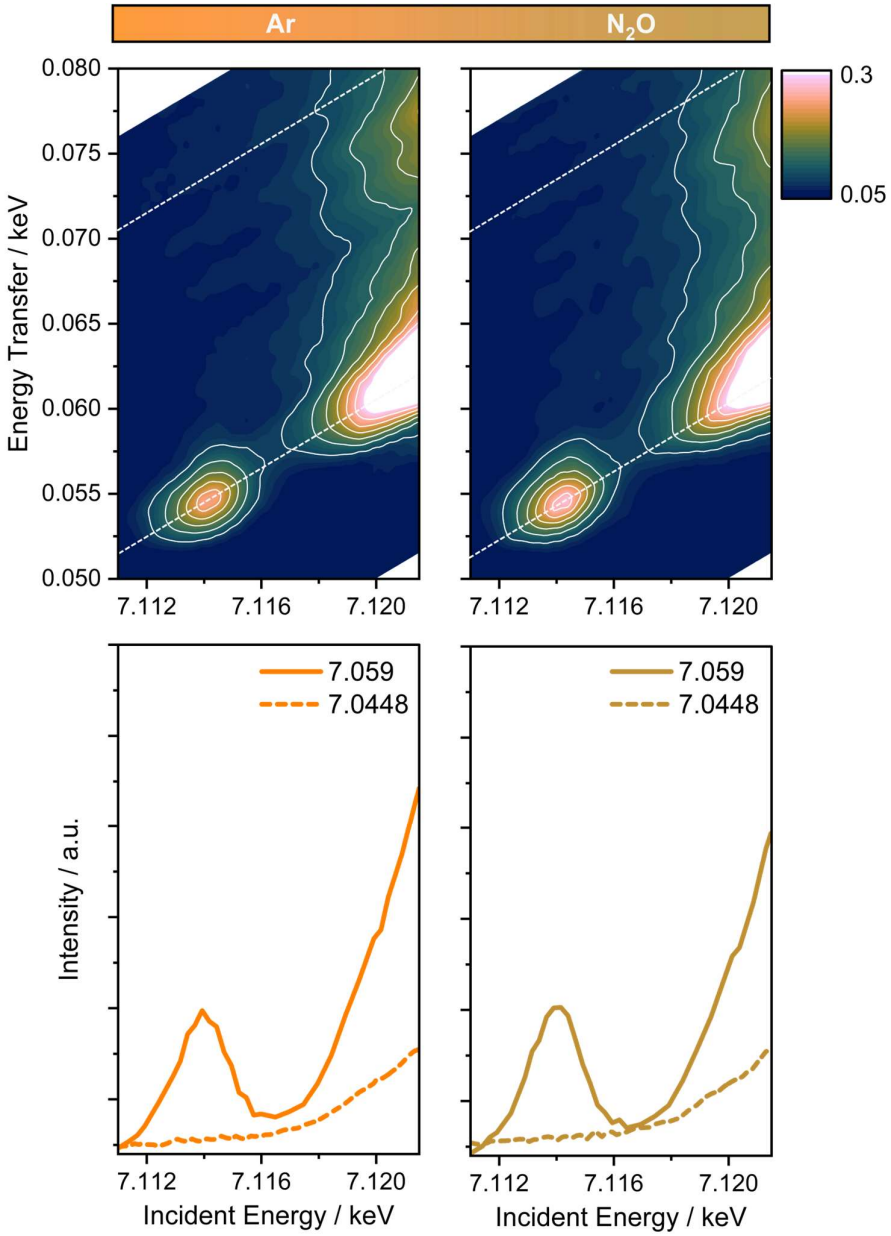

Supplementary Figure 16. Temporal evolution of the normalized ion current for the detected mass fragments m/z = 16 (CH_4), m/z = 44 (N_2O), m/z = 22 (carbon fragment), and m/z = 31 (CH_3OH), during CH_4 exposure in the *operando* XAS experiment (**Fig 3a**). Experimental conditions: total flow rate of 60 mL·min^{-1}, balanced in Ar, at 275°C, sequential exposure to N_2O (1 vol%) for 10 min (shown in **Supplementary Fig. 13**) followed by CH_4 (2 vol%) for 10 min.

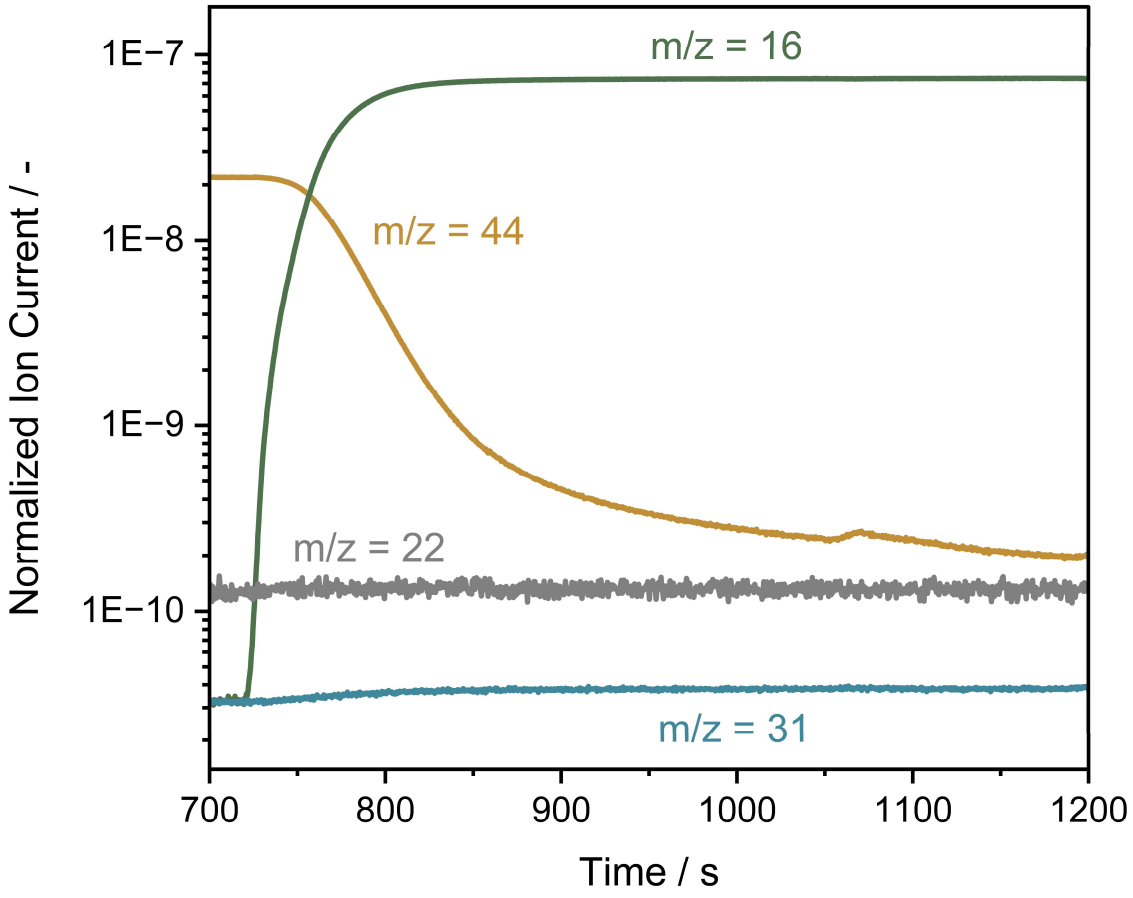

Supplementary Figure 17. Product distribution measured by μGC during the CH_4-only and N_2O + CH_4 co-feed steps of the *operando* DRIFTS experiments shown in **Fig. 3g**, highlighting the detectable gas-phase products. Experimental conditions: total flow rate of 60 $mL \cdot min^{-1}$, balanced in Ar, at 275°C, sequential exposure to N_2O (1 vol%) for 10 min (not shown), CH_4 (2 vol%) for 10 min, N_2O (0.5 vol%) + CH_4 (1 vol%) for 20 min, and finally Ar for 5 min.

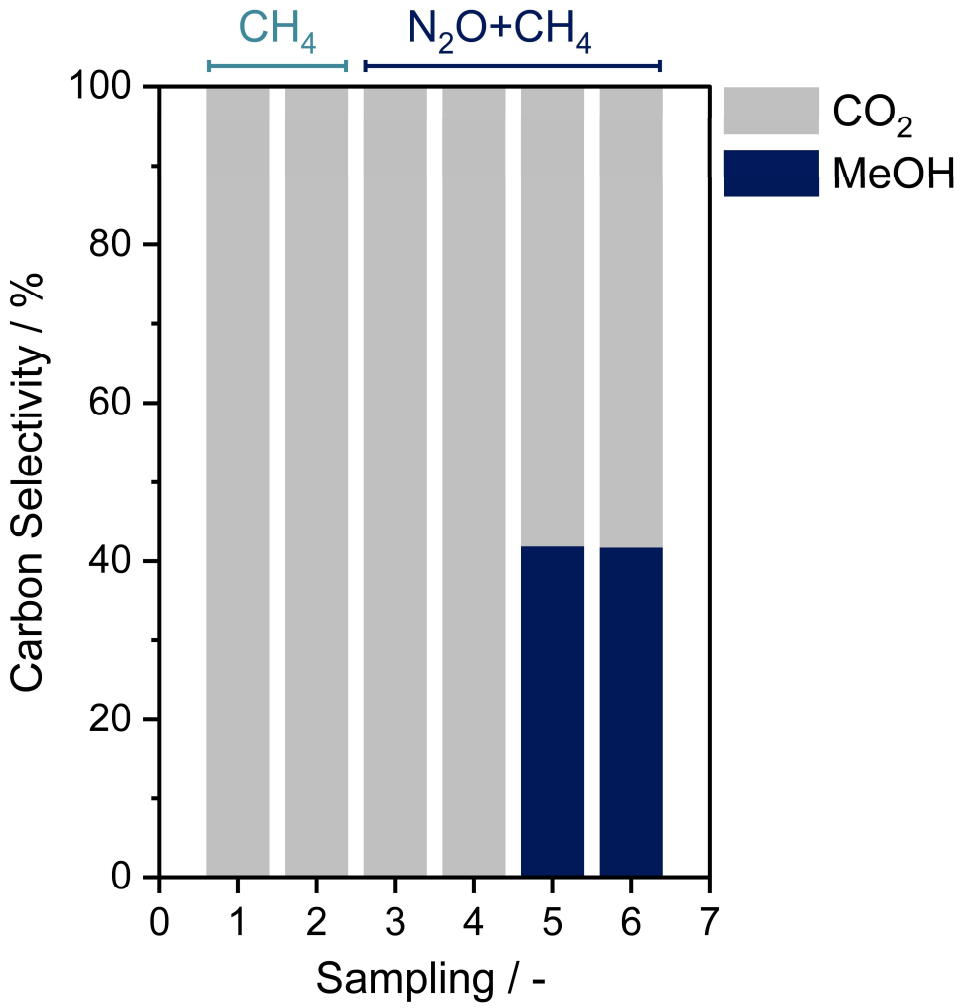

Supplementary Figure 18. Temporal evolution of the normalized ion current for the mass fragments m/z = 16 (CH_4), m/z = 44 (N_2O), m/z = 22 (carbon fragment), and m/z = 31 (CH_3OH), during N_2O + CH_4 co-feed in the *operando* XAS experiment (**Fig. 3a**). Experimental conditions: total flow rate of 60 mL·min^{-1}, balanced in Ar, at 275°C, N_2O (0.5 vol%) and CH_4 (1 vol%) for 20 min.

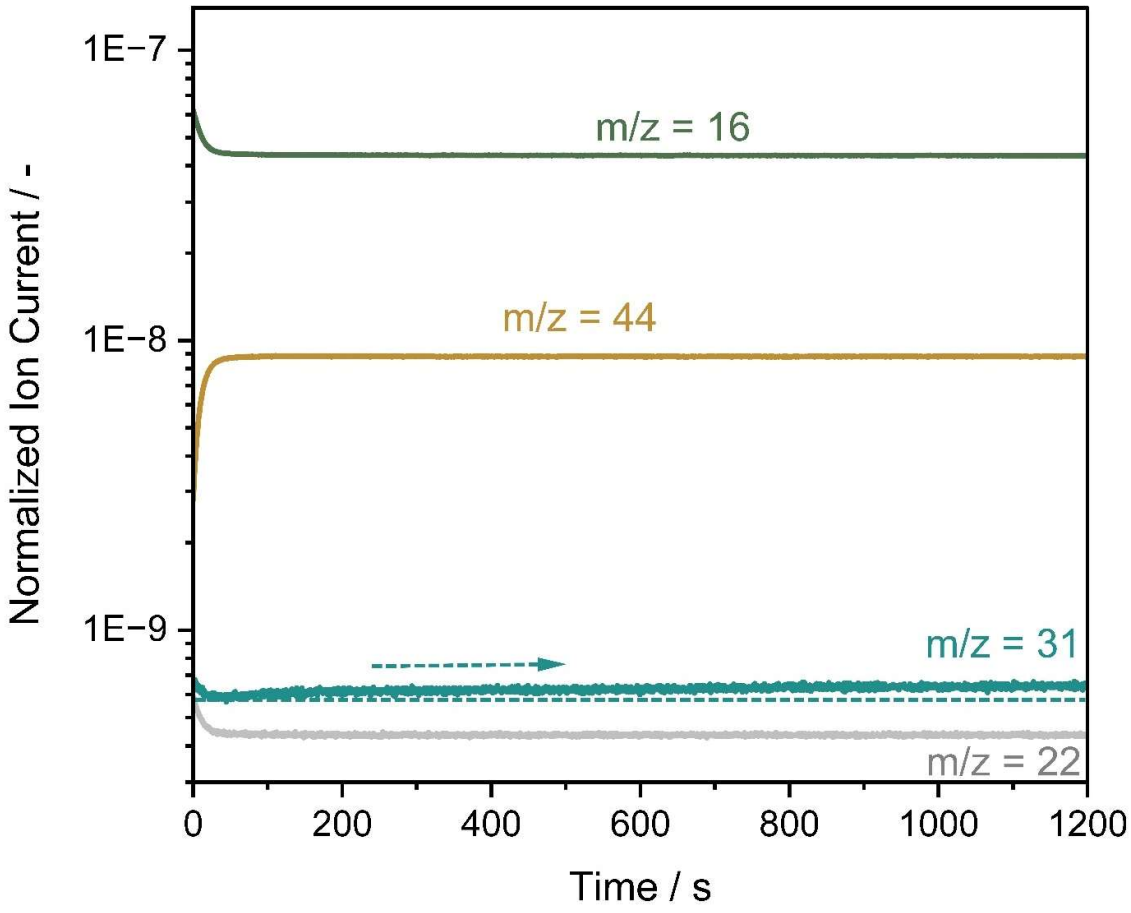

Supplementary Figure 19. Temporal evolution of the normalized ion current for the mass fragments m/z = 16 (CH_4), m/z = 18 (H_2O), m/z = 44 (N_2O), m/z = 22 (carbon fragment), and m/z = 31 (CH_3OH), during N_2O + CH_4 co-feed in the *operando* DRIFTS experiment (**Fig. 3g**). Experimental conditions: total flow rate of 60 mL·min^{-1}, balanced in Ar, at 275°C, N_2O (0.5 vol%) and CH_4 (1 vol%) for 20 min.

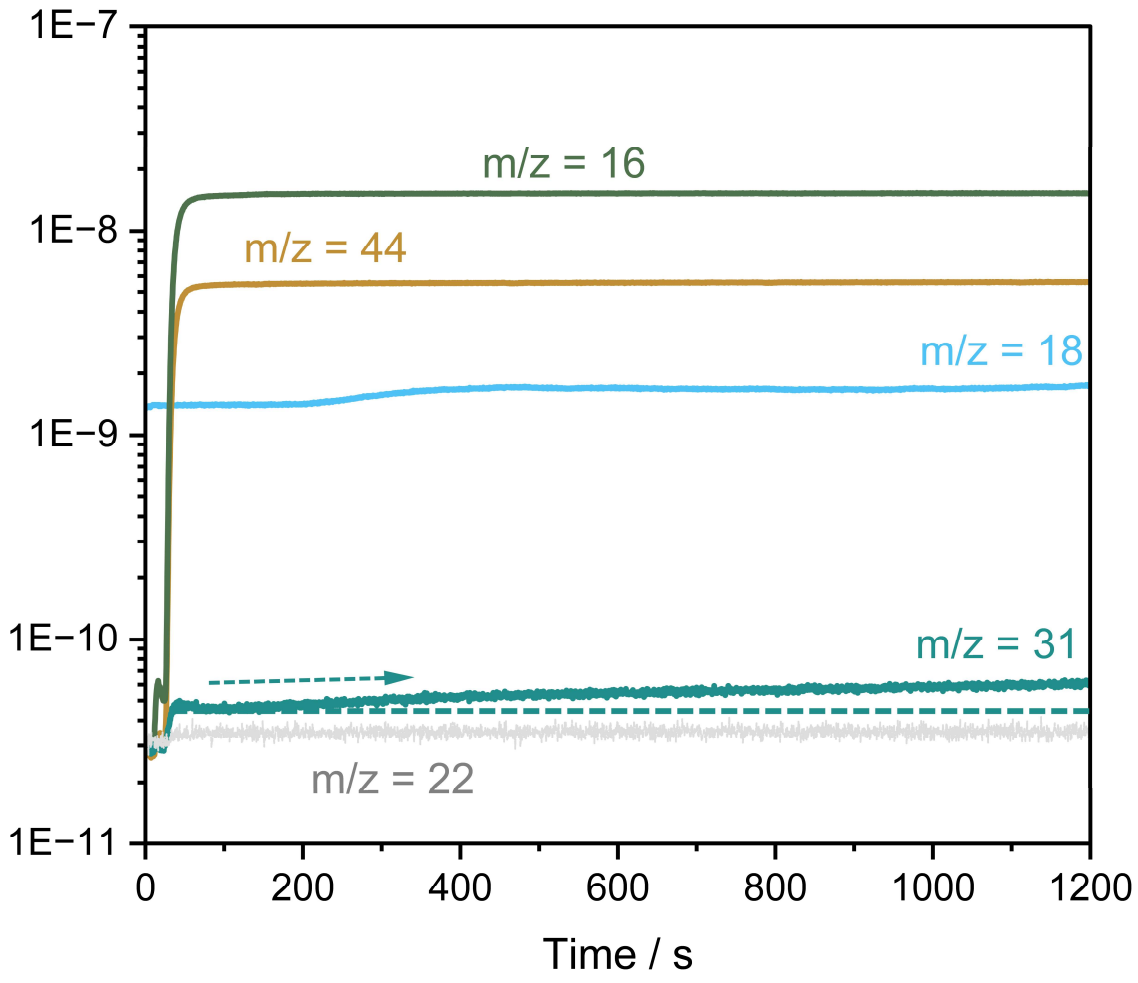

Supplementary Figure 20. Normalized intensity at fixed energy (7.1117, 7.1144, and 7.1201 keV) as a function of phase angle, recorded during ME-Kα-HERFD. Experimental conditions: total flow rate of 60 mL·min^{-1}, balanced in Ar, at 275°C, with 10 min pulses of CH_4 (1 vol%) introduced into a steady flow containing N_2O (0.5 vol%).

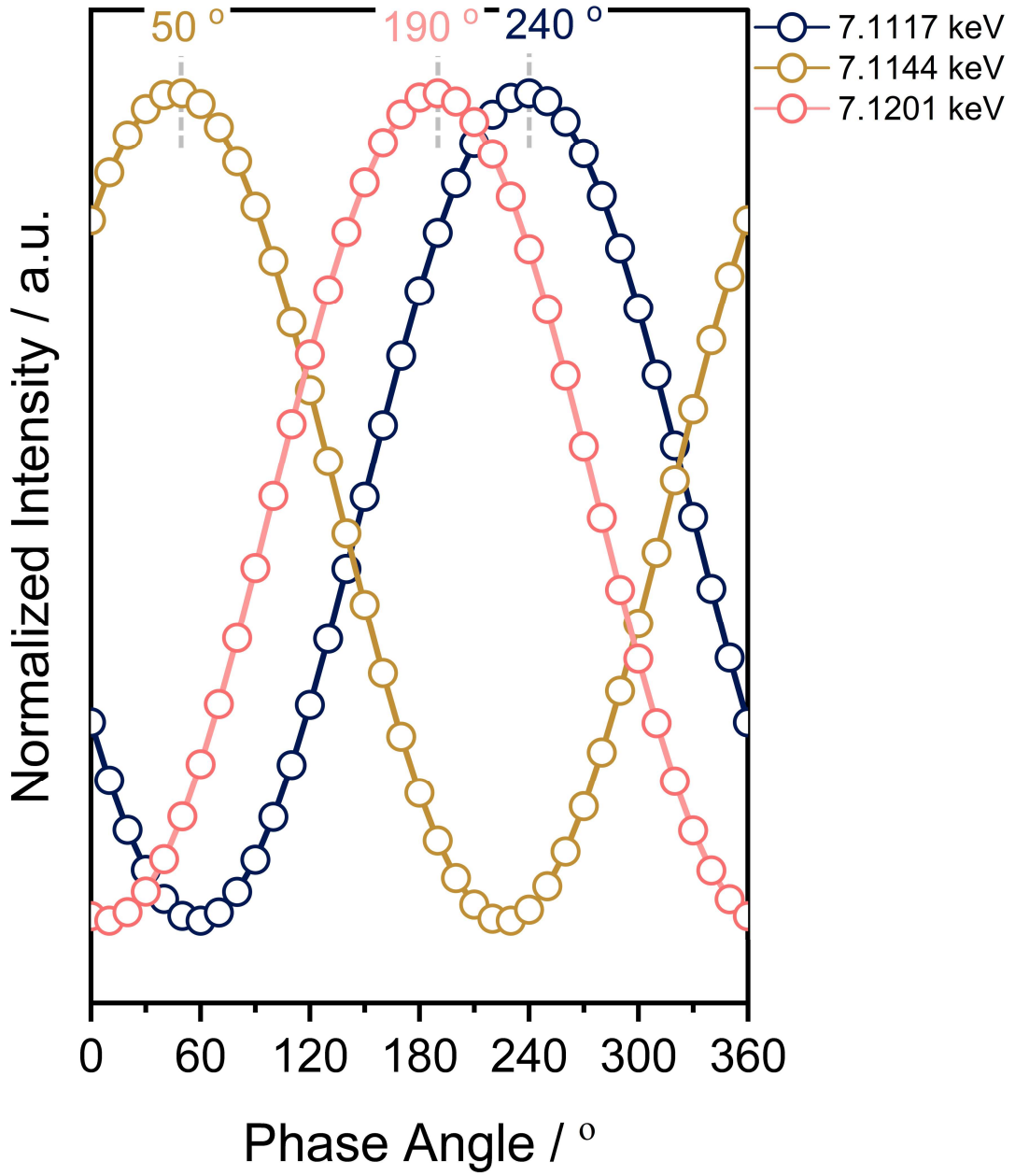

Supplementary Figure 21. Normalized pseudo-absorbance as a function of phase angle for selected vibrational bands at 2817, 2852, 2918, 2966, and 3662 cm^{-1}, recorded during ME-DRIFTS experiments. Experimental conditions: total flow rate of 60 $mL \cdot min^{-1}$, balanced in Ar, at 275°C, with 10 min pulses of CH_4 (1 vol%) introduced into a steady flow containing N_2O (0.5 vol%).

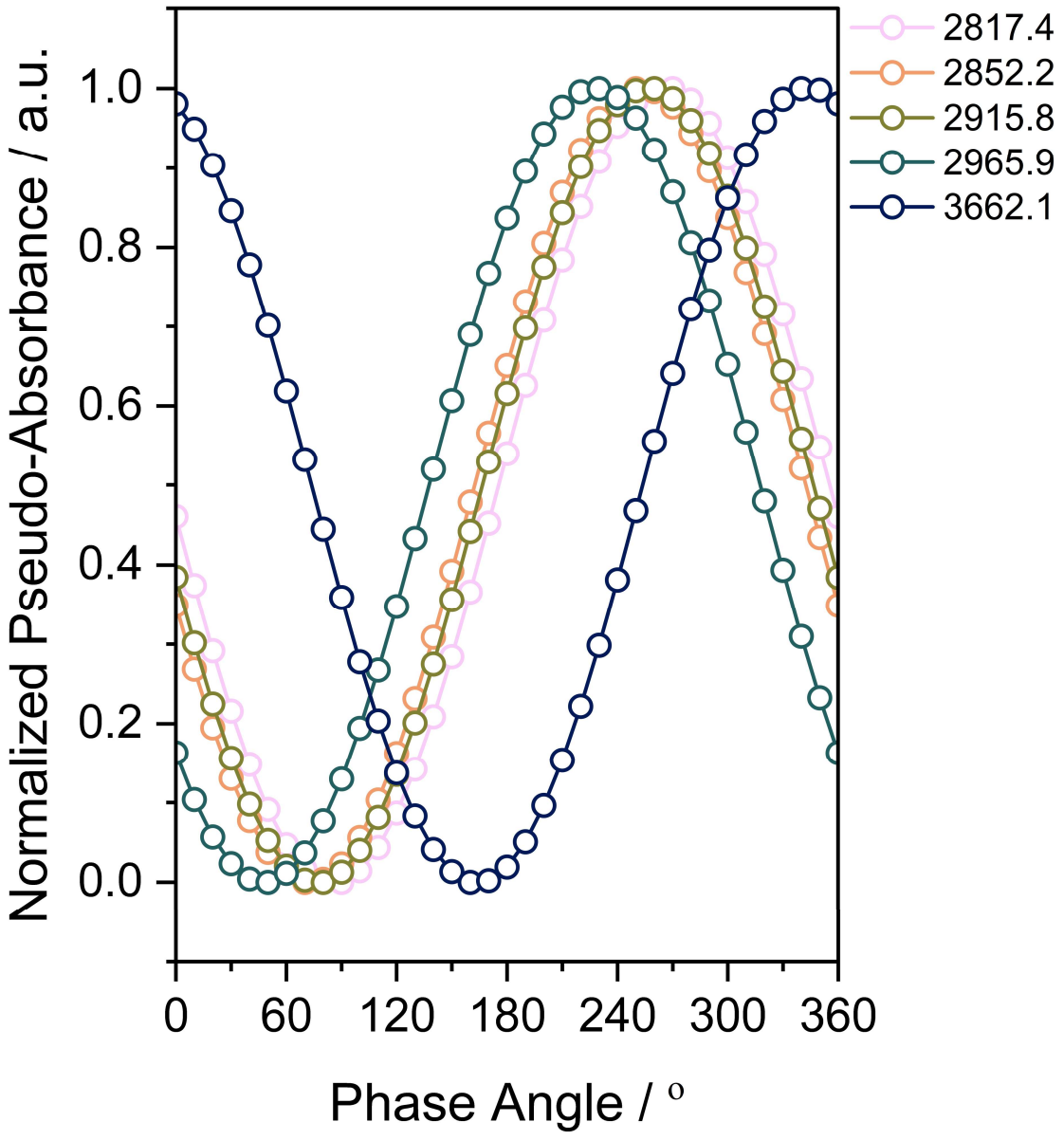

Supplementary Figure 22. Time evolution of the normalized ion currents for the detected mass fragments during the *operando* ME-DRIFTS experiment (**Fig. 4d**), showing two modulation periods. Monitored signals are m/z = 16 (CH_4), m/z = 18 (H_2O), m/z = 44 (N_2O), m/z = 12 (carbon fragment), m/z = 32 (MeOH), and m/z = 31 (MeOH), representing two of the modulation periods. Experimental conditions: total flow rate of 60 $mL \cdot min^{-1}$, balanced in Ar, at 275°C, with 10 min pulses of CH_4 (1 vol%) introduced into a steady flow containing N_2O (0.5 vol%).

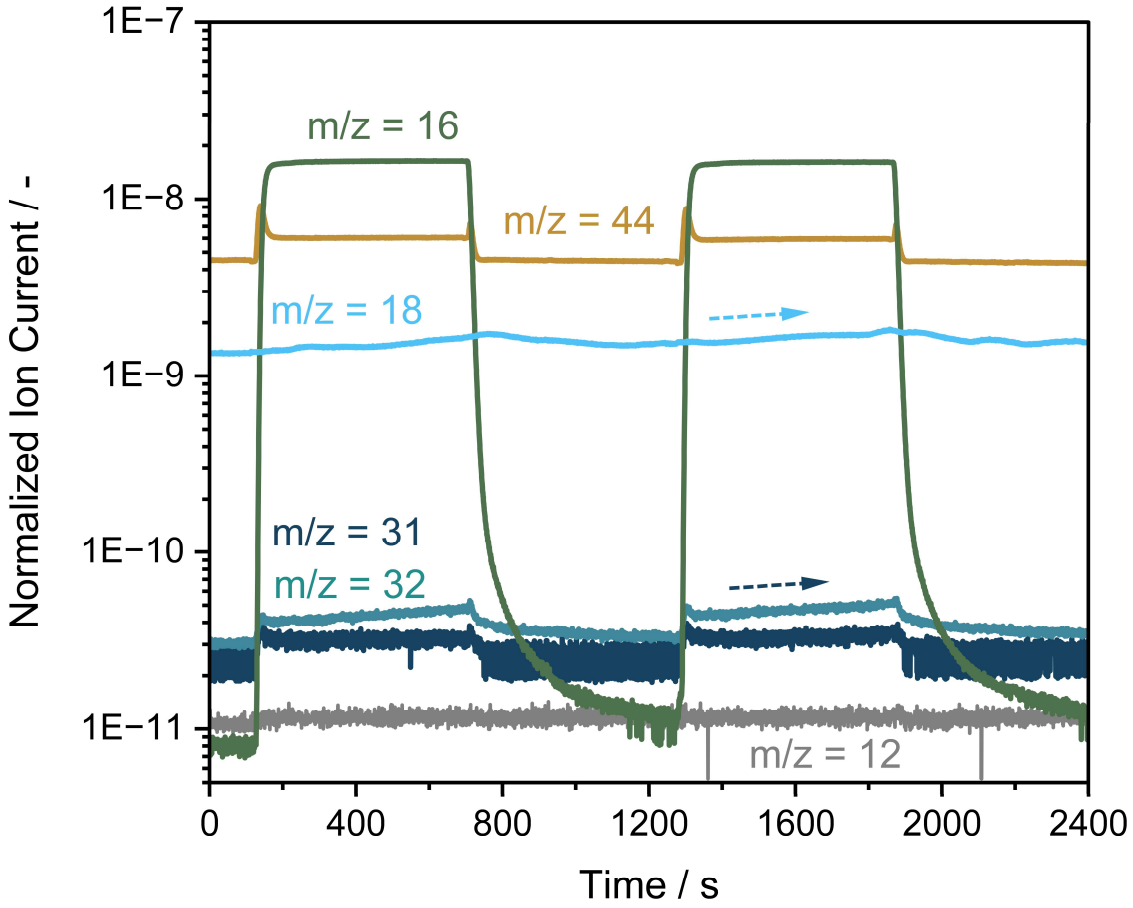

Supplementary Figure 23. Time evolution of the lack of fit, reported as the R factor (%), for the multivariate curve resolution fit of the time-resolved XANES spectra.

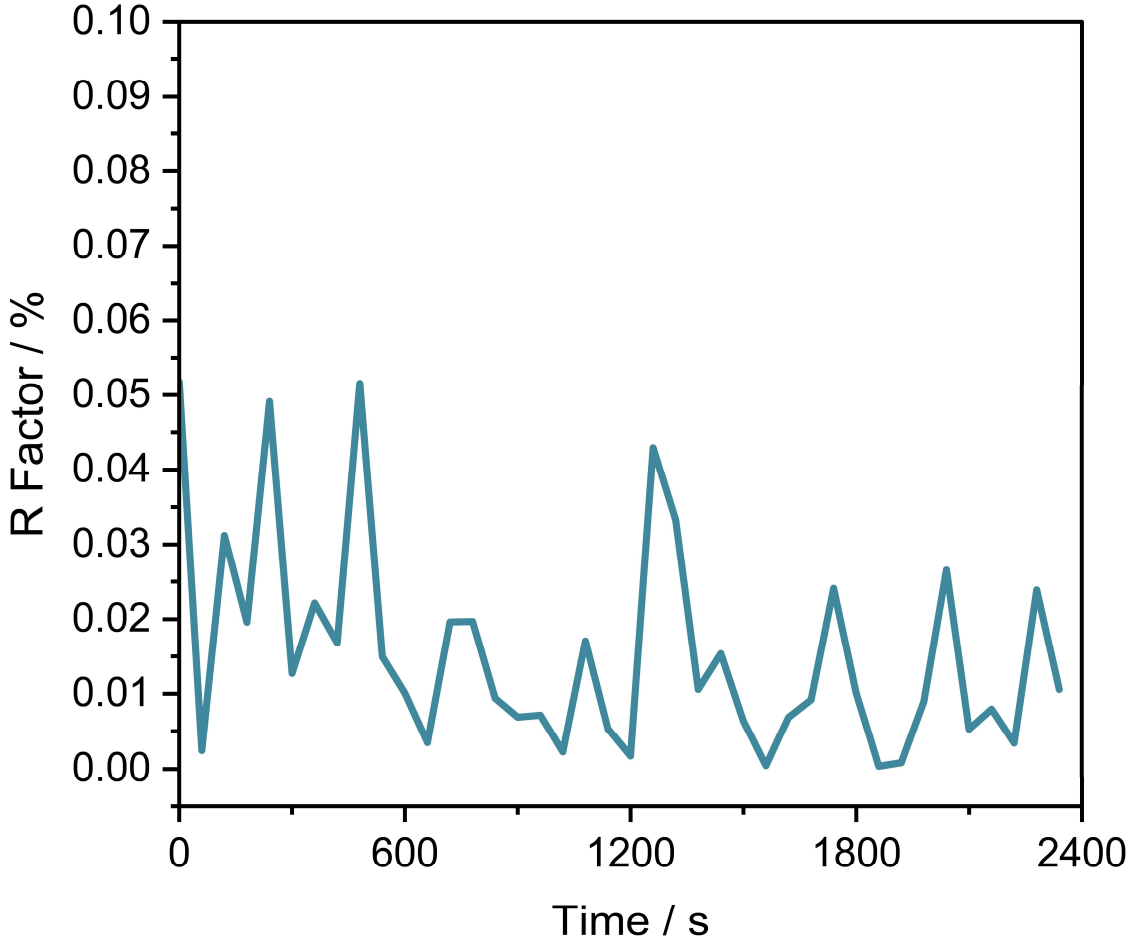

Supplementary Figure 24. Experimental protocol applied during the catalytic activity test. After thermal activation in Ar (heating to 420°C at 10 °C·min^{-1}, then holding for 30 min), the catalyst was cooled to the reaction temperature (275 °C). The feed was then switched sequentially to N_2O (30 min), CH_4 (30 min), and N_2O + CH_4 (2.5 h), while maintaining constant temperature.

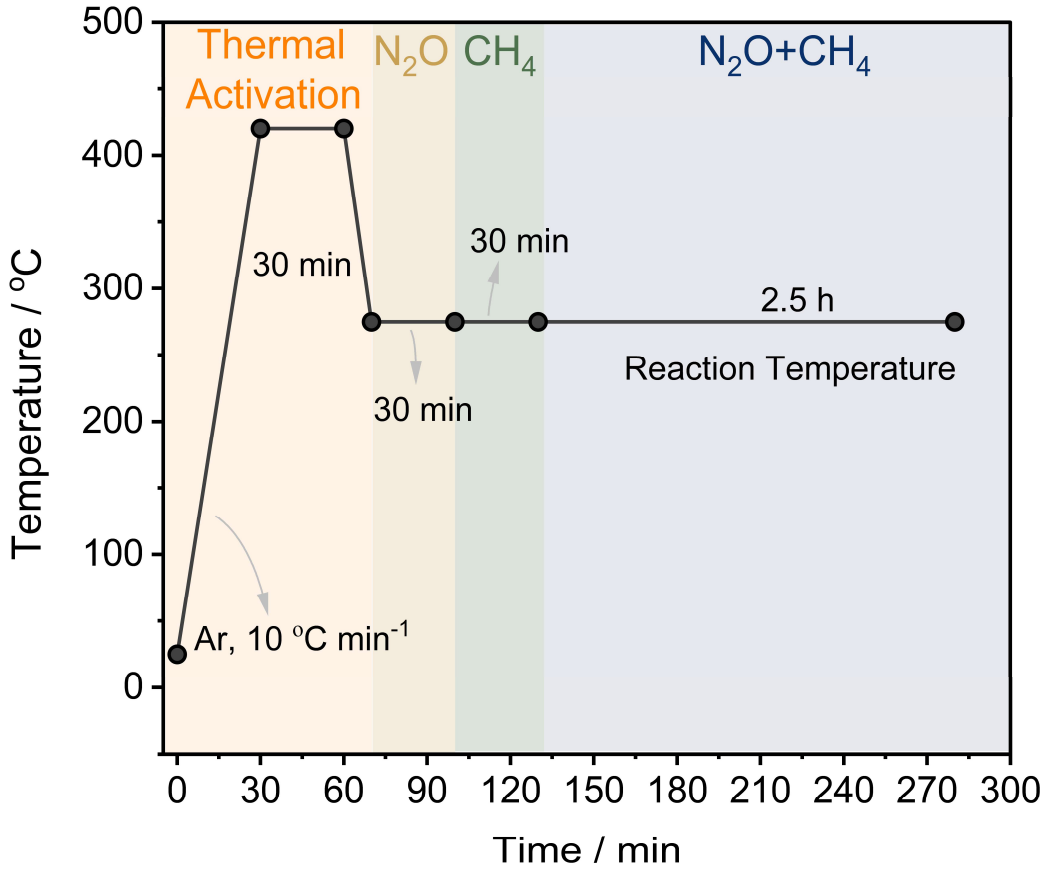

Supplementary Figure 25. Protocols used for the transient and modulated excitation (ME) spectroscopic experiments. Top: The catalyst was activated in Ar (10°C·min^{-1} to 420 °C, 30 min), cooled to 275 °C, and then exposed to N_2O (10 min), CH_4 (10 min), N_2O + CH_4 (20 min), and Ar (5 min). Bottom: During ME, N_2O was held constant at 0.5 vol%, while CH_4 was switched between 0 and 1 vol% every 10 min over n cycles, followed by Ar.

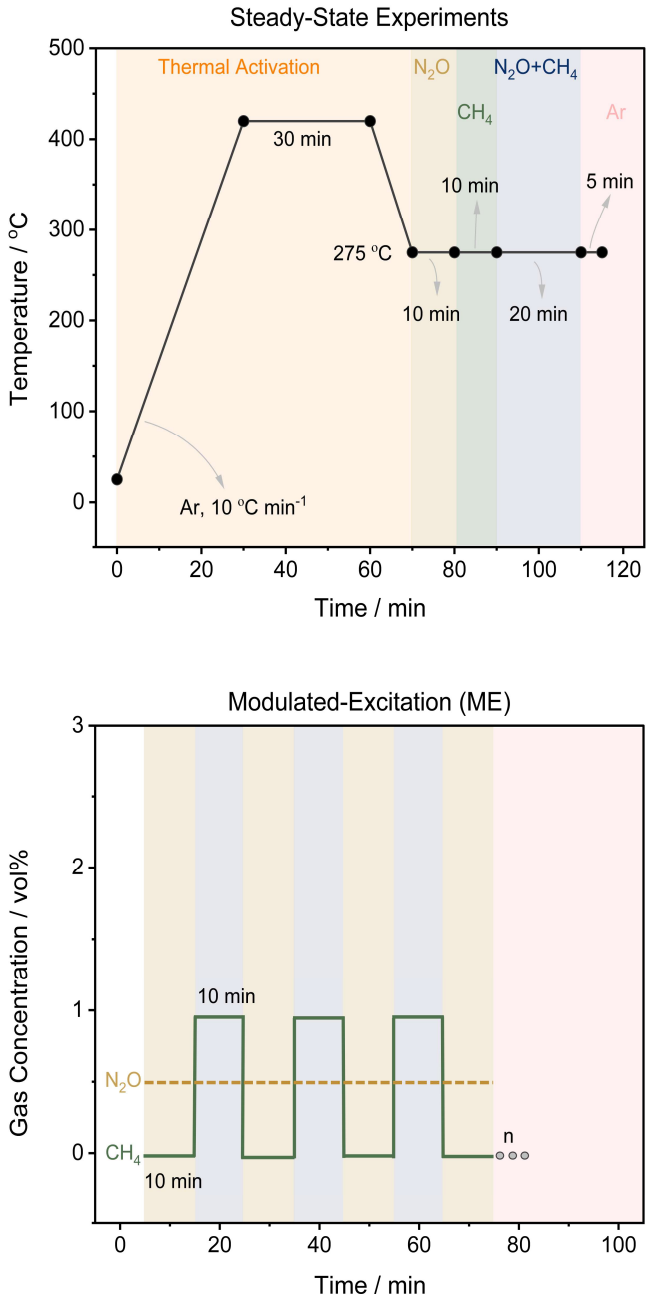

Supplementary Figure 26. Hexagonal CHA unit cells with two Al substitutions in the same 6MR and exchanged **a**, Fe^{2+} (Z_2Fe^{2+}) and **b**, $Fe^{3+}OH$ ($Z_2Fe^{3+}OH$). Yellow: Si; red: O; magenta: Al; white: H; and gray: Fe.

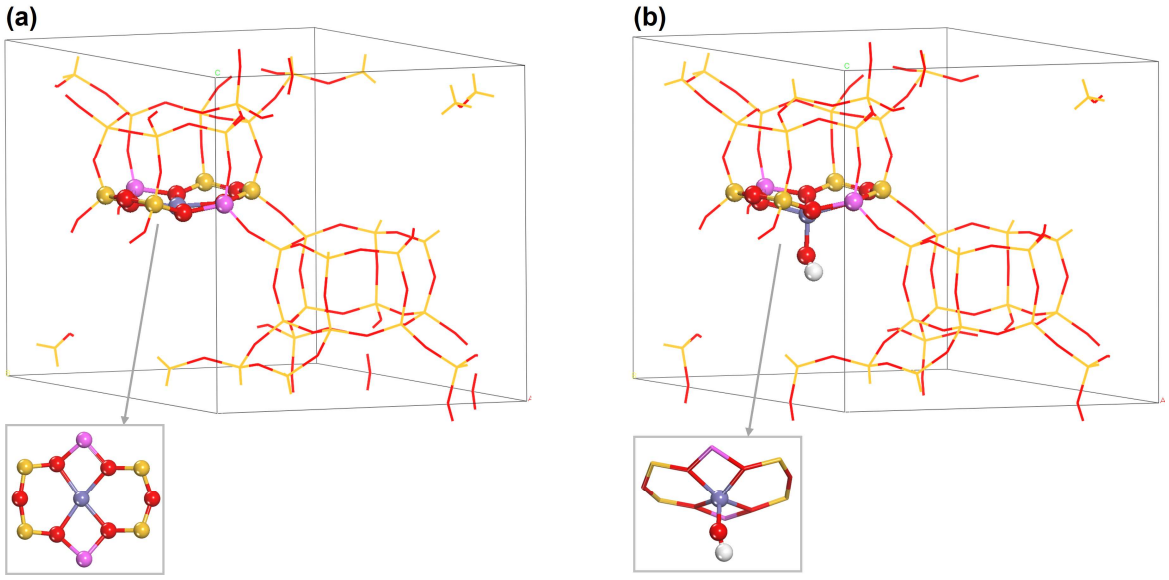

Supplementary References

1. Wilke M, Farges Fo, Petit P-E, Brown GE, Jr., Martin Fo. Oxidation state and coordination of Fe in minerals: An Fe K-XANES spectroscopic study. Am. Mineral. **86**, 714–730 (2001).

2. Boubnov A, Carvalho HWP, Doronkin DE, Günter T, Gallo E, Atkins AJ, et al. Selective Catalytic Reduction of NO Over Fe-ZSM-5: Mechanistic Insights by Operando HERFD-XANES and Valence-to-Core X-ray Emission Spectroscopy. J. Am. Chem. Soc. **136**, 13006–13015 (2014).

3. Westre TE, Kennepohl P, DeWitt JG, Hedman B, Hodgson KO, Solomon EI. A Multiplet Analysis of Fe K-Edge 1s → 3d Pre-Edge Features of Iron Complexes. J. Am. Chem. Soc. **119**, 6297–6314 (1997).

4. Simons MC, Prinslow SD, Babucci M, Hoffman AS, Hong J, Vitillo JG, et al. Beyond Radical Rebound: Methane Oxidation to Methanol Catalyzed by Iron Species in Metal–Organic Framework Nodes. J. Am. Chem. Soc. **143**, 12165–12174 (2021).

5. Simons MC, Vitillo JG, Babucci M, Hoffman AS, Boubnov A, Beauvais ML, et al. Structure, Dynamics, and Reactivity for Light Alkane Oxidation of Fe(II) Sites Situated in the Nodes of a Metal–Organic Framework. J. Am. Chem. Soc. **141**, 18142–18151 (2019).

6. C. Baerlocher, McCusker L. Database of Zeolite Structures. Available from: https://www.iza-structure.org/databases/

7. Bols ML, Hallaert SD, Snyder BER, Devos J, Plessers D, Rhoda HM, et al. Spectroscopic Identification of the alpha-Fe/alpha-O Active Site in Fe-CHA Zeolite for the Low-Temperature Activation of the Methane C-H Bond. J. Am. Chem. Soc. **140**, 12021–12032 (2018).

8. Snyder BER, Bols ML, Rhoda HM, Plessers D, Schoonheydt RA, Sels BF, et al. Cage effects control the mechanism of methane hydroxylation in zeolites. Science **373**, 327–331 (2021).

9. Kresse G, Furthmuller J. Efficient iterative schemes for ab initio total-energy calculations using a plane-wave basis set. Phys. Rev. B **54**, 11169–11186 (1996).

10. Kresse G, Joubert D. From ultrasoft pseudopotentials to the projector augmented-wave method. Phys. Rev. B **59**, 1758–1775 (1999).

11. Perdew JP, Burke K, Ernzerhof M. Generalized gradient approximation made simple. Phys. Rev. Lett. **77**, 3865–3868 (1996).

12. Meng Y, Liu XW, Huo CF, Guo WP, Cao DB, Peng Q, et al. When Density Functional Approximations Meet Iron Oxides. J. Chem. Theory Comput. **12**, 5132–5144 (2016).

13. Dudarev SL, Botton GA, Savrasov SY, Humphreys CJ, Sutton AP. Electron-energy-loss spectra and the structural stability of nickel oxide: An LSDA+U study. Phys. Rev. B **57**, 1505–1509 (1998).

14. Heyd J, Scuseria GE, Ernzerhof M. Hybrid functionals based on a screened Coulomb potential. J. Chem. Phys. **118**, 8207–8215 (2003).

15. Heyd J, Scuseria GE. Efficient hybrid density functional calculations in solids: assessment of the Heyd-Scuseria-Ernzerhof screened Coulomb hybrid functional. J. Chem. Phys. **121**, 1187–1192 (2004).

16. Heyd J, Scuseria GE, Ernzerhof M. Hybrid functionals based on a screened Coulomb potential (vol 118, pg 8207, 2003). J. Chem. Phys. **124** (2006).

17. Li S, Wang Y, Wu T, Schneider WF. First-Principles Analysis of Site- and Condition-Dependent Fe Speciation in SSZ-13 and Implications for Catalyst Optimization. ACS Catal. **8**, 10119–10130 (2018).

18. Grimme S, Antony J, Ehrlich S, Krieg H. A consistent and accurate ab initio parametrization of density functional dispersion correction (DFT-D) for the 94 elements H-Pu. J. Chem. Phys. **132**, 154104 (2010).

19. Grimme S, Ehrlich S, Goerigk L. Effect of the damping function in dispersion corrected density functional theory. J. Comput. Chem. **32**, 1456–1465 (2011).

20. Henkelman G, Arnaldsson A, Jonsson H. A fast and robust algorithm for Bader decomposition of charge density. Comput. Mater. Sci. **36**, 354–360 (2006).

21. Sanville E, Kenny SD, Smith R, Henkelman G. Improved grid-based algorithm for Bader charge allocation. J. Comput. Chem. **28**, 899–908 (2007).

22. Tang W, Sanville E, Henkelman G. A grid-based Bader analysis algorithm without lattice bias. J. Phys.: Condens. Matter **21**, 084204 (2009).

23. Chen L, Janssens TVW, Vennestrøm PNR, Jansson J, Skoglundh M, Grönbeck H. A Complete Multisite Reaction Mechanism for Low-Temperature NH3-SCR over Cu-CHA. ACS Catal. **10**, 5646–5656 (2020).

24. Cramer CJ. Essentials of computational chemistry: theories and models, 2nd edn. Wiley: Chichester, West Sussex, England; Hoboken, NJ, 2004.

25. Kwon S, Deshlahra P, Iglesia E. Reactivity and selectivity descriptors of dioxygen activation routes on metal oxides. J. Catal. **377**, 692–710 (2019).

26. Kwon S, Lin TC, Iglesia E. Elementary steps and site requirements in formic acid dehydration reactions on anatase and rutile TiO2 surfaces. J. Catal. **383**, 60–76 (2020).

27. Hu W, Iacobone U, Gramigni F, Zhang Y, Wang X, Liu S, et al. Unraveling the Hydrolysis of Z2Cu2+ to ZCu2+(OH)− and Its Consequences for the Low-Temperature Selective Catalytic Reduction of NO on Cu-CHA Catalysts. ACS Catal. **11**, 11616–11625 (2021).

28. Hu W, Selleri T, Gramigni F, Fenes E, Rout KR, Liu S, et al. On the Redox Mechanism of Low-Temperature NH3-SCR over Cu-CHA: A Combined Experimental and Theoretical Study of the Reduction Half Cycle. Angew. Chem. Int. Ed. **60**, 7197–7204 (2021).

29. Paolucci C, Parekh AA, Khurana I, Di Iorio JR, Li H, Albarracin Caballero JD, et al. Catalysis in a Cage: Condition-Dependent Speciation and Dynamics of Exchanged Cu Cations in SSZ-13 Zeolites. J. Am. Chem. Soc. **138**, 6028–6048 (2016).

30. Henkelman G, Jonsson H. Improved tangent estimate in the nudged elastic band method for finding minimum energy paths and saddle points. J. Chem. Phys. **113**, 9978–9985 (2000).

31. Henkelman G, Jonsson H. A dimer method for finding saddle points on high dimensional potential surfaces using only first derivatives. J. Chem. Phys. **111**, 7010–7022 (1999).

32. Xiao P, Nakamura K, Lu Y, Huang J, Wang L, Osuga R, et al. One-Pot Synthesized Fe-AEI Zeolite Catalysts Contribute to Direct Oxidation of Methane. ACS Catal. **13**, 16168–16178 (2023).

33. Gokce I, Ozbek MO, Ipek B. Conditions for higher methanol selectivity for partial CH4 oxidation over Fe-MOR using N2O as the oxidant and comparison to Fe-SSZ-13, Fe-SSZ-39, Fe-FER, and Fe-ZSM-5. J. Catal. **427**, 115113 (2023).

34. Zhao G, Benhelal E, Adesina A, Kennedy E, Stockenhuber M. Comparison of Direct, Selective Oxidation of Methane by N2O over Fe-ZSM-5, Fe-Beta, and Fe-FER Catalysts. J. Phys. Chem. C **123**, 27436–27447 (2019).

35. Chow YK, Dummer NF, Carter JH, Williams C, Shaw G, Willock DJ, et al. Investigating the influence of acid sites in continuous methane oxidation with N2O over Fe/MFI zeolites. Catal. Sci. Technol. **8**, 154–163 (2018).

36. Parfenov MV, Starokon EV, Pirutko LV, Panov GI. Quasicatalytic and catalytic oxidation of methane to methanol by nitrous oxide over FeZSM-5 zeolite. J. Catal. **318**, 14–21 (2014).

37. Cano-Blanco DC, Fischer JWA, Buttignol F, Alxneit I, Jeschke G, Kröcher O, et al. Monomeric Fe in Six-Membered Rings at Work: Operando Spectroscopy of Nitrous Oxide Activation and Decomposition over Fe-Exchanged Zeolites. ACS Catal. **15**, 15579–15595 (2025).

38. Fischer JWA, Cano-Blanco DC, Karas H, Buttignol F, Kröcher O, Ferri D, et al. Disentangling Site-Selective Redox Couples for N2O Activation on Fe-Exchanged SSZ-13 Using Modulated Excitation Operando EPR Spectroscopy. ChemCatChem **18**, e01575 (2026).